

1 **TITLE: CRB3 and ARP2/3 regulate cell biomechanical properties to set epithelial**
2 **monolayers for collective movement.**

3 **Authors : Dominique Massey-Harroche¹, Vito Conte^{2, 3, 4}, Niels Gouirand¹, Michäel Sebbagh⁵,**
4 **André Le Bivic¹, Elsa Bazellières^{1*}**

5

6 1 : Aix Marseille Univ, CNRS, Institute of Developmental Biology of Marseille IBDM UMR 7288,
7 Campus de Luminy, case 907, 13288, Marseille cedex 09, France

8 2 : Institute for Bioengineering of Catalonia (IBEC), The Barcelona Institute of Science and
9 Technology (BIST), Barcelona – Spain

10 3 : Institute for Complex Molecular Systems (ICMS), Eindhoven University of Technology
11 (TU/e), Eindhoven – the Netherlands

12 4 : Department of Biomedical Engineering, Eindhoven University of Technology (TU/e),
13 Eindhoven – the Netherlands

14 5: Centre de Recherche en Cancérologie de Marseille, CRCM, Aix Marseille University, Institut
15 Paoli-Calmettes, CNRS, INSERM, 'Cell Polarity, Cell Signaling and Cancer'- Equipe Labellisée
16 Ligue Contre le Cancer, Marseille, France.

17 *: corresponding author: elsa.bazellieres@univ-amu.fr

18

19

20

21 **Abbreviations :**

22 ABP (apico-basal polarity), EMP (Epithelial to Mesenchymal Plasticity), CRB3 (Crumbs3), PALS1
23 (Protein Associated with Lin Seven 1), PATJ (PALS1-Associated Tight Junction), ARP2/3 (Actin
24 Related Protein 2/3 complex), KD (knockdown), PDMS (Polydimethylsiloxane)

25

26

27 **Summary**

28

29 Several cellular processes during morphogenesis, tissue healing or cancer progression involve
30 epithelial to mesenchymal plasticity that leads to collective motion (plasticity?). Even though
31 a rich variety of EMP programs exist, a major hallmark unifying them is the initial breaking of
32 symmetry that modifies the epithelial phenotype and axis of polarity. During this process, the
33 actin cytoskeleton and cellular junctions are extensively remodelled correlating with the build-
34 up of mechanical forces. As the collective migration proceeds, mechanical forces generated
35 by the actin cytoskeleton align with the direction of migration ensuring an organized and
36 efficient collective cell behaviour, but how forces are regulated during the breaking of
37 symmetry at the onset of EMP remains an unaddressed question. It is known that the polarity
38 complex CRB3/PALS1/PATJ, and in particular, CRB3 regulates the organization of the actin
39 cytoskeleton associated to the apical domain thus pointing at a potential role of CRB3 in
40 controlling mechanical forces. Whether and how CRB3 influences epithelial biomechanics
41 during the epithelial-mesenchymal plasticity remains, however, largely unexplored. Here, we
42 systematically combine mechanical and molecular analyses to show that CRB3 regulates the
43 biomechanical properties of collective epithelial cells during the initial breaking of symmetry
44 of the EMP. CRB3 interacts with ARP2/3 and controls the remodelling of actin throughout the
45 monolayer via the modulation of the Rho-/Rac-GTPase balance. Taken together, our results
46 identified CRB3, a polarity protein, as a regulator of epithelial monolayer mechanics during
47 EMP.

48

49 **Introduction**

50 Epithelia are cohesive layers of apico-basally polarized (ABP) cells that adhere and
51 communicate with each other through specialized intercellular junctions and with the
52 substrate through focal adhesions ¹⁻³. During development and in some diseases such as
53 cancer, epithelial tissues can perform either complete epithelial to mesenchymal transitions
54 or partial epithelial to mesenchymal transition that has been redefined as epithelial to
55 mesenchymal plasticity ⁴⁻⁸. The early phase of EMP mechanically relies on the ability of cells
56 to break their symmetry switching from an apico-basal conformation to a front-rear
57 polarization.

58 The remodeling of epithelial cells at the periphery of the monolayer requires : i) cell spreading
59 ^{9,10}, by extending basal actin protrusion such as lamellipodia to explore the free space; and, ii)
60 cell migration, by constantly remodeling the focal adhesions that anchor the actin stress fibers
61 at the substrate ¹¹⁻¹⁷. During this initiation of migration, a well-balanced coordination of
62 protrusive and retractive forces needs to be maintained by each individual cell that compose
63 the monolayer sheet. Once engaged in the migration process, the leader cells pull via their
64 intercellular adhesions on the follower cells which in turn gradually begin to spread and
65 migrate ^{18,19}. Theoretical and analytical studies suggest that the leader cells might induce
66 normal strain on the follower cells and shear stress on adjacent cells, translating a local stress
67 to coordinated traction forces and cell polarization, which finally results in coordinated motion
68 ²⁰⁻²². So far, many studies have focus on the molecular mechanisms that controls the
69 mechanical forces when the cells are already migrating ^{1,16,21,23-28}. Despite extensive studies,
70 the molecular mechanisms that govern the breaking of symmetry of EMP together with the
71 forces underlying this process remains still elusive. In terms of biology during EMP, the
72 remodeling of the cell-cell adhesions, cell matrix adhesions and the reorganization of the actin
73 cytoskeleton correlate with the relocation of the CRB3 polarity complex proteins to the
74 migrating cell front (review in ^{12,29-31}). The canonical CRB (Crumbs) complex, in mammals is
75 composed of CRB3/Protein Associated with Lin Seven 1 (PALS1) and PALS1-Associated Tight
76 Junction (PATJ) and is known to regulate the actin cytoskeleton organization and intercellular
77 adhesions. CRB is the only protein to possess a transmembrane domain among the polarity
78 complexes, and it has been shown to regulate the organization of intercellular adhesions and
79 actin cytoskeleton in *Drosophila*, zebrafish and mouse embryos ²⁹. CRB3 has been shown to
80 play an important function in the establishment and the maintenance of cellular apico-basal
81 polarity ³²⁻³⁵, whereas PALS1 and PATJ have been shown to be explicitly involved in the process
82 of collective cell migration ^{33,36-38}. Furthermore, all these data strongly suggest a role for the
83 CRB3 polarity complex in EMP. We still ignore, however, how CRB3 protein and its partners
84 function during the breaking of symmetry of EMP ³⁹⁻⁴².

85 Here, we systematically study how CRB3 and its partners impact the epithelial monolayer
86 architecture and mechanics during EMP. We found that CRB3 in tandem with Arp2/3 regulate
87 the breaking of symmetry during the epithelial transition. We have also shown that CRB3 is
88 required for actin remodeling through a permissive effect on Rac1 activation, thereby

89 promoting actin fiber remodeling and alignment along with focal adhesion maturation and
90 orientation and force alignment.

91

92 **Results**

93

94 **Initial breaking of symmetry of EMP leads to actin cytoskeleton remodeling and apical** 95 **polarity complex relocation**

96 We have developed a new experimental pipeline to reproducibly monitor the biomechanical
97 behavior of an epithelial monolayer transitioning from a static differentiated epithelial
98 morphology to a migratory phenotype. As a cell model system, we adopted the Caco-2 human
99 intestinal cells as they establish a robust ABP when reaching confluency^{43–45} and actively
100 spread and migrate on free substrates^{46–48}. We used soft lithography to fabricate thin
101 polydimethylsiloxane (PDMS) membranes with a rectangular opening, which we laid on top of
102 a soft polyacrylamide gel substrate coated with collagen-I (Fig. 1A). After 20hr of culture (time
103 t=0 hour), Caco2 cells formed a confluent polarized and symmetric epithelial monolayer and
104 display a cuboidal shape (Fig. 1A, B-E). At this stage, the actin cytoskeleton is organized in well-
105 defined structures running from the apical to the basal domain of the cells. At the apical side
106 of the cells, a dense brush border made by microvilli is observed (Fig. 1 B, red asterisk), along
107 with a lateral cortical actin belt that bridges the cellular junctions (Fig. 1C, green arrowhead).
108 At the basal side of cells, instead, stress fibers are formed (Fig. 1 D) and an actin cable is visible
109 (Fig. 1 D, blue arrowhead) that connects the free cell fronts at the monolayer's edge.
110 Classically, CRB3, PALS1 and PATJ are mainly located apically at lateral junctions (Fig.1H-J, K,-
111 M, N-0 top left graph, black arrow)⁴⁹.

112 10hr after PDMS stencil removal, the monolayer apico-basal symmetry is broken at free edges,
113 and the epithelial layer flattens (Fig. 1, E', F) and spreads (Fig. 1 C', G,). There, cells acquire a
114 migratory state and develop an elongated shape in the epithelial plane. Basally, the actin cable
115 observed at 0hr has vanished, while lamellipodia and actin arcs form (Fig. 1 D', yellow
116 arrowhead). The data show that the actin cytoskeleton is extensively remodeled during the
117 symmetry breaking, when the free edge cells initiate transition. Moreover, despite the
118 presence of well-defined junctional cortical actin (Fig. 1 C', green arrowhead), no brush border
119 could be detected, and only sparse microvilli are observed at the apical surface (Fig. 1 B', red

120 asterisk), thus suggesting a remodeling of the ABP state of free edge cells. Interestingly, actin
121 re-organization correlates with a drastic change in the subcellular localization of the CRB3
122 polarity complex during EMP. Although PALS1 and PATJ remained located at the lateral
123 junctional belt (Fig1 I' and J' green arrowhead, L', M', O, P bottom left graph, black arrow), a
124 significant pool became redistributed at the lamellipodial membrane (white arrowhead Fig 1I',
125 J' white arrowhead, L', M', O, P bottom left graph blue arrow, O, P right graph). In sharp
126 contrast, junctional CRB3 was barely detected at the junction at this stage, and the protein
127 rather accumulated in intracellular vesicles and focal accumulations at the lamellipodia edge
128 (Fig. 1 H' white arrowheads, K', N bottom left graph blue arrow, N right graph). These data
129 show that the remodeling of the ABP state of free edge cells triggers the recruitment of the
130 CRB3 polarity complex during monolayer symmetry breaking, albeit with a different
131 distribution between PALS1/PATJ and CRB3. In conclusion, apico-basal symmetry breaking at
132 the free edge of the epithelium triggers the relocalization of the CRB3 polarity complex, which
133 correlates with the remodeling of the actin cytoskeleton,

134

135 **CRB3 is required for the epithelial transition to collective migration.**

136 In order to test the function of CRB3 polarity complex in epithelial transition, we selectively
137 silenced the expression of CRB3, PALS1 and PATJ using siRNA approach (Fig. S1) and utilized
138 our experimental set up to quantify monolayer migration efficiency (Fig. 2A-E). Phase contrast
139 microscopy revealed that control monolayers (siCT) and siPALS1 knock-down (KD) monolayers
140 are able to migrate efficiently (Fig. 2A, B, E blue and purple curves), with siPALS1 migrating to
141 further extents than the siCT cells (Fig. 2A, B, E). In contrast, depletion of PATJ or CRB3
142 significantly reduces the monolayer migration (Fig. 2C, D, E green and red curves). Specifically,
143 siCRB3 monolayers exhibit the strongest phenotype with a 2-fold reduction of migration
144 efficiency compared to controls (Fig. 2E, red curve).

145 In addition, after 10hr, we observed a defect in the cell protrusions at the free edge of
146 depleted monolayers (Fig. 2A-D, yellow asterisks, bottom panels). In the absence of PATJ, a
147 milder phenotype is observed, with $45,7\% \pm 4,2\%$ (Fig. 2F, green undashed box plots) of
148 leading-edge cells forming protrusions, while CRB3 depletion drastically affected the number
149 of membrane protrusions since only $19,1\% \pm 3,2\%$ of leading-edge cells bear protrusions (Fig.
150 2F, red undashed plots). Taken together, these data demonstrate a pivotal role for CRB3 in
151 the breaking of symmetry during epithelial transition, and prompt us to further characterize

152 the cell protrusion defects observed in CRB3-KD monolayers. Analysis of the leading edges at
153 10hr showed actin filament mis-organization in the absence of CRB3 (Fig.2 G, H, middle panel
154 insets), together with mis-localization of ARP2/3 (Fig. 2 G,H, top panel white arrowheads and
155 inset). In fact, a thick actin cable is formed in CRB3-KD monolayer edges. In addition, ARP2/3
156 is not further recruited at the protrusion cortex in the mutant free edge cells. Subcellular
157 fractionation and Western blot experiments further confirmed global decrease expression of
158 ARP2/3 associated with the membrane in the absence of CRB3, while the total expression level
159 of ARP2/3 is not affected (Fig.2I, J). Collectively, these results testify of the absence of
160 lamellipodia formation in the absence of CRB3. We thus postulated that the absence of CRB3
161 may hamper actin remodeling at the cell membrane, preventing the branching of actin and
162 promoting the accumulation of bundled/contractile actin at the monolayer free edge during
163 epithelial transition.

164

165 **CRB3 promotes Rac1 activation and actin branching for proper epithelial transition to**
166 **collective migration.**

167 One way to regulate the branched versus the bundled/contractile actin network is by
168 controlling the balance of Rac1 and Rho small GTPases, with Rac1 activation triggering
169 branching of actin via activation of ARP2/3, and Rho activation favoring the
170 bundled/contractile actin^{50,51}. To measure the level of activation of these small GTPases in
171 CRB3 depleted cells, we performed a GST-pull down assay with GST fused to Rhotekin-
172 p21Binding Domain (GST-Rhot-PBD) or PAK-p21Binding Domain (GST-PAK-PBD) to pull down
173 activated Rho or activated Rac, respectively, in both control and siCRB3 cells (Fig. 3A-C). CRB3
174 depleted-cells have less activated Rac (Fig. 3 A top panel, B) while Rho activation is increased
175 (Fig. 3 A bottom panel, C), when compared to control cells. These data show a perturbation in
176 the balance of small GTPase activity, with Rho hyperactivation together with Rac
177 hypoactivation in cells depleted of CRB3. This phenotype is compatible with the absence of
178 formation of lamellipodia observed in siCRB3 at the monolayer free edges, and strongly
179 suggest a specific defect in the remodeling of branched actin.

180 We further assessed whether a direct link exists between branched actin remodeling and
181 symmetry breaking during epithelial transition. As expected from literature^{52,53}, inhibiting
182 actin branching with CK666 drug treatment or using siARP2/3 transfection blocks the

183 formation of cell protrusion and prevents the global migration of the epithelial control
184 monolayer (Fig. 3D-H). These results nicely mimicked the CRB3 depletion phenotype we
185 observed in Figure 2. In addition, ARP2/3 has been shown to directly interact with CRB3 in
186 Sertoli cells⁵⁴. We thus investigated whether CRB3 binding to ARP2/3 also takes place in our
187 system. By using affinity-precipitation (peptide pull-down) with the full-length cytoplasmic
188 domain of CRB3 (90-120 AA, CRB3 cyt) or the same cytoplasmic domain only containing the
189 FERM binding domain (90-100 AA, CRB3FERMBD) that binds to cytoskeletal associated
190 proteins such as ARP2/3⁵⁴ (Fig. S2A), we revealed that ARP2/3 interacts with CRB3-FERM
191 binding domain construct (Fig. S2B).

192 To determine whether a functional correlation exists between CRB3 and ARP2/3 for branched
193 actin remodeling, we scrutinized actin fiber arrangement in siCT, siCRB3 and siARP2/3 cells at
194 0hr and 10hr after removing the PDMS stencil (Fig 4). Whereas CRB3 or ARP2/3 silencing did
195 not affect the initial organization of actin cytoskeleton (Fig. 4 A-C, S3), differences appear
196 between siARP2/3, siCRB3 cells and siCT cells after 10hr of PDMS removal (Fig. 4 A'-C', S3). In
197 a similar manner, both siCRB3 and siARP2/3 cells do not exhibit lamellipodia but instead still
198 display a thick actin cable at their free basal edge (Fig 4 B',C' blue arrowhead). These data
199 clearly state that the phenotypes observed result from a defect in the disassembly and
200 remodeling of the actin cytoskeleton. Further segmentation of the actin filaments and
201 quantitative analysis of their organization in the basal cell leading edge revealed that no clear
202 difference could be noted between the 3 conditions at 0hr (Fig 4D-F, G-H dashed boxes). At
203 10hr, however siARP2/3 cells developed a thick actin cable oriented orthogonally to the
204 migration direction (Fig 4 F', blue inset), as siCRB3 cells did (Fig.4E', blue inset). In addition,
205 quantification of alignment coherence and orientation index, where 0 reflects an orientation
206 of the fibers in the direction of migration and 1 reflects an orientation of the fibers
207 perpendicular to the direction of migration (see Materials and Methods), shows a reduced
208 orientation index and less coherent alignment of actin fibers in siCRB3 and siARP2/3 at 10h
209 compared to control cells (Fig.4 E', F', G, H undashed boxes). These quantifications reflect a
210 loss of the polarized state of the monolayer at the free edge in siCRB3 and siARP2/3 cells. All
211 together, these data show that CRB3 and ARP2/3 are both needed for the correct organization
212 of the actin fibers tangentially to the direction of migration. As remodeling of the actin
213 cytoskeleton is coupled to changes in cell shape, it can be thus considered as the deformability

214 potential of cells ^{55,56}. We therefore computed the cell area, height and use the changes in
215 cell area as a proxy to compute the strain rate of cell spreading (Fig. S3). Control cells
216 presented a high rate of deformation in spreading with a strain rate of 4,35 demonstrating
217 that Caco-2 cells strongly remodel their shape when they start to migrate at 10hr (Fig S3K). In
218 sharp contrast, a quasi-null strain rate of 0,89 and 1,16 was computed for siCRB3 and siARP2/3
219 cells respectively (Fig S3K), siCRB3 and siARP2/3 cells being taller and expanding less than
220 controls (Fig. S3A'-I', J undashed box, M). Our data shows that CRB3 together with ARP2/3 are
221 essential for the remodeling of epithelial cell shape, and in particular for cell spreading, during
222 the initial transition from epithelial to migrating cells through the remodeling of the actin
223 cytoskeleton.

224 In summary, using a variety of tools, we have shown that CRB3 is required for cells to properly
225 activate Rac1 and remodel the actin cytoskeleton in a similar way to the actin branching
226 protein ARP2/3.

227

228 **CRB3 and ARP2/3 regulate the remodeling of cell-matrix adhesions**

229 The remodeling of the actin cytoskeleton is required for the cell-substrate adhesion (review
230 in ⁵⁷). We therefore decided to study the focal contacts in our system, to decipher a potential
231 correlation between the organization of the actin filaments and the organization of the focal
232 adhesions. Focal adhesions were immunostained for paxillin, at 0hr and 10hr after removal of
233 the PDMS membrane in the different depletions (Fig. 5A-C, A'-C'), and image segmentation
234 and analyses of the focal contacts were performed to measure their maximal length, size
235 repartition orientation (Fig. S4, Fig.5 G, H) and spatial dispersion of focal contacts (Fig.5D-F,
236 D'-F', I). Moreover, as previous works have shown that, as cells start to migrate, their focal
237 contacts are remodeled and matured from small nascent adhesion to larger focal adhesions
238 ^{58,59}, we subdivided accordingly the focal adhesions into three different categories: nascent
239 $<0.25\mu\text{m}$, focal complex $<0.5\mu\text{m}$, focal adhesions $>1-5\mu\text{m}$ ⁵⁷. Therefore, by looking at the ratio
240 of the different adhesion categories at 0hr and 10hr, we addressed whether the focal contacts
241 are able to be remodeled and matured from nascent to focal adhesions. At 0hr, no significant
242 difference was measured in the different conditions, indicating that focal adhesions were not
243 affected by any of the depletions when the cells are in a static epithelial state (Fig. 5A-C, G-H,
244 dashed boxplots). At 10hr, an increase in size with a higher ratio of mature focal adhesions

245 was observed in siCT cells (Fig 5G, S4G). As siCT cells spread, the length of the actin filament
246 increased and this was translated by an increase in the dispersion of the focal adhesion (Fig 5
247 D-D', I undashed blue box). At the opposite, siCRB3 and siARP2/3 cells exhibited an opposite
248 trend with smaller immature focal contacts (Fig. 5G, undashed boxplot), and a significant
249 decrease of their orientation and dispersion (Fig. 5 H-I, undashed boxplot) in comparison with
250 control cells.

251 In conclusion, defects in shape, orientation and distribution of focal adhesions in siCRB3 and
252 siARP2/3 cells showed the requirement of CRB3 together with ARP2/3 in remodeling focal
253 contacts, and may be explained by a defective remodeling and growth of the basal actin fibers.

254

255 **Loss of CRB3 or ARP2/3 perturbs the mechanics of the cellular monolayer**

256 Actin dynamics and focal adhesions are related to force generation and transmission across
257 epithelial cell monolayers^{31,60}. We thus postulate that CRB3 together with ARP2/3 could be
258 involved in the generation and alignment of forces that are required for the cells to initiate
259 efficient collective motion²⁰⁻²².

260 Traction force microscopy and monolayer stress microscopy^{20,21,23} were used to measure
261 forces that cells exert at the surface of the substrate. To visualize the orientation and
262 alignment of tension, we plot the vectorial fields of tension. At 0hr, before the symmetry
263 breaking, tractions exhibited a punctate pattern with higher tractions forces being exerted
264 toward the edge of the monolayer in control cells as in siCRB3 and siARP2/3 cells, with
265 depleted cells exhibiting overall higher tractions (Fig.6D-F). In a similar manner, tensions are
266 higher in siCRB3 and siARP2/3 cells compared to control cells (Fig. 6 G-I) and exhibit lower
267 anisotropy as represented by the orientation of maximal force tensor (Fig. 6J-L). After 10hr,
268 traction forces and tension increase with cells depleted for CRB3 and ARP2/3 exerting higher
269 forces in comparison with controls (Fig.6D'-F', G'-I'). Interestingly, the anisotropy of the
270 maximal force tensor increases as the vectors tend to align toward the direction of migration
271 in control cells (Fig 6J'). In contrast, in siCRB3 and siARP2/3, we still observed strong anisotropy
272 and disorganization of the vectors at 10hr (Fig. 6K', L'). To give a comprehensive understanding
273 on how the mechanics evolved in response to the different siRNAs, we computed the temporal
274 evolution of tension, tractions, and of the Shannon's entropy in the vectorial fields. This

275 analysis revealed that control cells, siCRB3 and siARP2/3 cells increased their tractions and
276 tension, albeit forces in siCRB3 and ARP2/3 being always higher than in control cells (Fig.6M,
277 N). Interestingly, cells depleted for CRB3 and ARP2/3, are not able to align their tension as the
278 control cells do, as shown by the increased entropy in siCRB3 and siARP2/3 cells (Fig.6 O).
279 Thus, depletion of CRB3 or ARP2/3 impacted the global mechanical properties, intensity and
280 organization, of the cell monolayer.

281 To further determine whether a correlation occurs between biological and mechanical
282 phenotypes, we selected morphometric parameters (cell area, cell orientation, cell
283 elongation, focal adhesion area, focal adhesion orientation, focal adhesion elongation, actin
284 fiber orientation and coherency) and mechanical parameters (monolayer kinetics, tractions,
285 tension and entropy) and summarized our data in two matrices (Fig. 7), 0hr and 10hr, for three
286 conditions, (Fig. 7A-D). We computed two matrices in which each element contains the z-score
287 of the morphometric and mechanical properties in response to each depletion. This numerical
288 analysis demonstrates that the mechanical parameters are markedly affected at 0hr for both
289 KD cell lines, while a relevant impact is not measured in the morphometric parameters. At
290 10hr, we observed a reinforcement of the mechanical properties along the same trends
291 observed at 0hr (Fig. 7B, D), while drastic modifications can be observed for the morphometric
292 properties (Fig. 7A, C).

293

294 Collectively, these data demonstrated the reciprocity between cell behavior and mechanical
295 features, and in particular, the relationship between the remodeling of actin
296 cytoskeleton/focal adhesions, and the loaded forces the cells exert at the cell-cell interface
297 and on their underlying substrate.

298

299 **Discussion**

300 Epithelia transition towards collective migration is associated with changes in cell polarity and
301 adhesion in epithelial tissues. The transition from a static monolayer to collective migration
302 begins with the breaking of symmetry from apical-basal to front-rear at the monolayer edge
303 and ends up with collective cell motion. These steps require a coordinated remodeling of
304 intercellular adhesions, focal contacts and actin cytoskeleton. In our study we have
305 implemented a system that allows the systematic study the transition from a static monolayer

306 where epithelial cells polarize in the ABP axis, to a more dynamic monolayer where leading
307 edge migrating cells develop instead front-to-rear polarized state.

308 Here we have identified CRB3 / ARP2/3 as mechanoregulatory module of the symmetry
309 breaking during EMP. Several studies performed on different cellular models, such as non-
310 tumorigenic human mammary epithelial cells, tumorigenic kidney-derived cells or colorectal
311 adenocarcinoma cells have led to conflicting conclusions regarding the function of CRB3
312 during collective cell motion³⁹⁻⁴². In human mammary epithelial cells or tumorigenic kidney
313 cells, the loss of CRB3 expression increases cell invasion, and promotes cell scattering while
314 our study together with the work of Lioka et al³⁹ clearly demonstrates that loss of CRB3
315 prevents cell spreading. The discrepancies between different cell lines might be explained by
316 different factors. Firstly, the regulation of protein expression such as CRB3 depends on the
317 model system used^{40,61-64}. Recently, it has been described that CRB3 gene expression differs
318 depending on the tumoral tissues or cell models^{39,61-63}. As an example, CRB3 is upregulated
319 in colorectal and breast cancer whereas in glioblastoma it is downregulated. In the study of
320 Mao et al⁶³, the authors also described that in non-tumorigenic breast MCF10A cells, CRB3
321 expression and localization depends on the cellular density with a lower expression in
322 confluent cells when compare to sparse cells. These different expression patterns could result
323 in the formation of distinct complexes, and trigger various signaling pathways that could lead
324 to a great variety of phenotypes. These differences should be considered before raising a
325 conclusion regarding the role of CRB3 during collective cell migration. Secondly, the choice of
326 the cellular model is crucial to address properly the question of the initial step of the transition
327 from a static differentiated epithelial to a migratory epithelial monolayer, when cells
328 dramatically change their polarity and shapes as well as their actin organization. Caco2 cells
329 are highly polarized with a dense apical actin network, forming a brush border, and robust
330 cellular adhesions, mimicking *in vivo* enterocyte organization. When cells start to spread, the
331 polarity proteins are relocalized, the apical actin network is disassembled and cellular
332 adhesions are remodeled, leading to a dramatic cell shape change. The study by Li et al, used
333 MCF10A mammary epithelial cells, which are not columnar, do not exhibit a dense apical actin
334 brush border and have weaker cellular adhesions^{61,64,65}. In the case of MCF10A cells, the
335 remodeling of the actin cytoskeleton is less drastic when compared to Caco2 cells, as the cells
336 do not undergo a massive change of shape. Therefore, the results obtained with this MCF10A

337 cell line cannot be generally transposed to understand the breaking of symmetry during EMP.
338 The Caco2 cell line used in the present study is a more suitable epithelial model to address the
339 regulation of the actin cytoskeleton during the initial cell spreading and allows us to unveil a
340 key role of CRB3 in this process.

341 Our study was, however, not limited to CRB3 but also identified new functional module for
342 EMP composed by CRB3 and ARP2/3. By performing a global quantitative analysis of several
343 biological and mechanical parameters, we were able to demonstrate with an unbiased
344 approach that CRB3 and ARP2/3 exhibit similar functions and could be part of the same
345 functional module during EMP. In line with this conclusion, our biochemical data also show
346 that CRB3 can bind to ARP2/3 independently of PALS1, confirming a heterogeneity of CRB3
347 complex composition. Using Caco2 cells, we describe ARP2/3 as a potential mechanobiological
348 effector of CRB3, and show that CRB3 expression regulates the small GTPase Rac/Rho balance.
349 CRB3 is essential for the cells to activate Rac1, and with ARP2/3 they promote the remodeling
350 of actin and the maturation focal adhesion during the breaking of symmetry of EMP. Previous
351 studies have shown a role of the CRB polarity protein complex in the regulation of the actin
352 cytoskeleton in other cellular processes ²⁹ and here we have found a new cellular context for
353 the role of CRB3 in regulating actin organization. CRB3 is a small transmembrane protein that
354 forms a polarity complex with PALS1 and PATJ which can both recruit regulatory proteins to
355 modulate actin organization. In our study we show, however, that CRB3 can interact with
356 ARP2/3 independently of PALS1 and PATJ, via its FERM binding domain. Our data suggests that
357 to break epithelial symmetry, CRB3 might be relocated to the leading edge where, as a
358 transmembrane protein, it recruits ARP2/3, an actin binding protein that is necessary for the
359 formation of protrusions. This localization leads to cell polarization with a polarized activation
360 of the Rho/Rac balance in a rear-to-front fashion depending on the localization of CRB3 as
361 proposed by several studies ^{18,29,66}. During this initial cell spreading, this local activation of Rac
362 induces cytoskeletal rearrangements with a rapid actin polymerization and alignment of the
363 actin filament promoting the engagement and maturation of focal contacts ⁶⁷, which in turn
364 correlates with a regulation of mechanical forces¹. By using traction forces microscopy and
365 Shannon entropy correlation analysis, we were able to quantitatively show that CRB3 is
366 needed to fine regulate the amount and alignment of forces. These data are in line with the
367 fact that during collective motion epithelial cells increase and align their forces^{20,22}, however,

368 similar behavior during the breaking of symmetry initiating epithelial transition was not
369 described so far.

370

371 To our knowledge, this is the first study that clearly links a polarity protein, CRB3, to the
372 remodeling and reorganization of the actin cytoskeleton and focal adhesions to the
373 mechanical regulation leading to the breaking of symmetry during the shift between static to
374 migrating epithelium, a key process in cell, developmental biology and mechanobiology.

375

376

377 **Figure Legends**

378 **Fig. 1: F-actin is remodeled and the polarity complex CRB3 is relocated during the onset of**
379 **EMP.** A) Scheme of the experimental set up and schematic representation of the organization
380 of the monolayer before and after migration. A PDMS membrane (in grey) is deposited on top
381 of a polyacrylamide gels. Cells are seeded within the rectangular opening and after 20hr the
382 PDMS membrane is removed. Just after removal of the PDMS membrane (0hr) the epithelial
383 cell monolayer is cuboidal and microvilli cover the apical domain, and after 10hr, cells flatten,
384 the microvilli are lost at the edge where lamellipodia form as represented in the drawing. The
385 different domains are represented together with the cellular junction and the actin
386 cytoskeleton. F-Actin organization at 0hr (B-D) and 10hr (B'-D') of migration. Red asterisks:
387 microvilli, yellow arrowhead: actin arcs, green arrowhead: lateral junctional actin, blue
388 arrowheads: thick actin cable. Lateral view of the F-actin organization at 0hr (E) and 10hr (E')
389 of migration. Scale bars= 10 μ m. F) Monolayer height as function of the distance from the
390 center of the cell monolayer. For the different time points several lateral views were measured
391 (0hr, n=44, grey line, 10hr, n= 44, black line). Data are presented as mean \pm SEM. G)
392 Quantification of cell area at 0hr (dashed box plot, n=162) and 10hr (empty box plots, n=127)
393 of migration. Data are presented as mean \pm Min Max. Localization of CRB3, PALS1, PATJ at 0hr
394 (H-J), and 10hr (H'-J') of migration. Scale Bar =10 μ m. White arrowheads point the leading edge
395 of the cell monolayer, green arrowheads point cell-cell adhesions, dashed lines point where
396 the intensity profiles shown in panel N-P are measured. Lateral view of the localization of
397 CRB3, PALS1 and PATJ at 0hr (K-M) and 10hr (K'-M') of migration. Scale bars= 10 μ m. N-P) On
398 the left panels, representative fluorescence intensity profile of CRB3 (N), PALS1 (O), PATJ (P)
399 at 0hr and 10hr. Black arrow point the junction of the cell, and blue arrow the peak detected
400 at the edges. On the right panels, quantification of the mean fluorescence intensity of CRB3
401 (N), PALS1 (O) and PATJ (P) at the edge of the monolayer at 0hr (dashed box plots) and 10hr

402 (empty box plots). For each siRNA 4 fields of views were quantified. Data are presented as
403 mean \pm Min Max.

404

405 **Fig. 2: Downregulation of the CRB3 polarity complex alters collective cell migration and the**
406 **formation of protrusions.** Representative phase contrast images showing the effect of each
407 siRNAs (control siCT (A), siPALS1 (B), siPATJ (C) and siCRB3 (D) on cell monolayer expansion at
408 0hr and 10hr of migration. Yellow asterisks: cell protrusions. Scale bar = 50 μ m. E) Time
409 evolution of monolayer expansion (shown as the distance covered by the cell monolayer from
410 the initial point). Number of monolayers for siCT blue, n =7; siPALS1, purple, n =4; siPATJ,
411 green, n=4, siCRB3, red, n=3. F) Cells at the leading-edge bearing protrusions. The box plots
412 represent the ratio between the number of protrusions to the number of cells at the leading
413 edge for each siRNAs at 0hr (dashed box plots) and 10hr (empty box plots) of migration.
414 Number of cells counted for siCT, blue, n=238 0hr, n=228 10hr; siPALS1, purple, n=150 0hr,
415 n=125 10hr; siPATJ, green, n=207 0hr, n=195 10hr; siCRB3, red, n=156 0hr, n=136 10hr. Data
416 are presented as mean \pm Min Max. Representative images of ARP2/3 and F-Actin
417 immunostaining in siCT (G), and siCRB3 (H) at 10hr. White arrowheads: edge of the monolayer.
418 Inset are representative zoomed region of ARP2/3 and F-actin immunostainings. Scale bars
419 10 μ m. I) Immunoblot analysis showing the expression of ARP2/3 5 days after transfections
420 with siCT and siCRB3. α -Tubulin was used to standardize the loading conditions between the
421 different depletions. Quantification of protein expression levels normalized to siCT cells. Data
422 are represented as mean \pm SEM. For each protein, n=3 samples pooled from 3 independent
423 transfections. J) Immunoblot analysis of membrane fraction purified lysate of ARP2/3 5 days
424 after transfection with siCT and siCRB3. α -Tubulin was used to standardize the loading
425 conditions between the different depletions. Quantification of protein expression levels
426 normalized to siCT cells. Data are represented as mean \pm SEM. For each protein, n=3 samples
427 pooled from 3 independent transfections

428

429 **Fig. 3: Rho/Rac balance are perturbed in CRB3 depleted cells, and inhibition of branched**
430 **actin mimic siCRB3 phenotype.**A) Representative western blot images showing the effect of
431 CRB3 downregulation on the activation of Rac (top panel) and Rho (bottom panel). siCT and
432 siCRB3 lysates were pulled-down with GST-CT, GST-PAK-PBD (top panel) and GST-Rhot-PBD
433 (bottom panel) and probed to detect Rac (top panel) and Rho (bottom panel) expression. The
434 activation of Rac (B) and Rho (C) were quantified by computing the ratio between the amount
435 of Rac and Rho pull-down to the total expression detected in the siCT and siCRB3 lysates. The
436 data presented in the histograms are the mean \pm SEM of 3 independent experiments for siCT
437 and 3 independent experiments for siCRB3. D-F) Representative phase contrast images
438 showing the expansion of siCT cells, siARP2/3 and siCT/CK666 treated cells at 10hr of
439 migration. Scale bar = 50 μ m. G) Cells at the leading-edge bearing protrusions. The box plots
440 represent the ratio between the number of protrusions to the number of cells at the leading

441 edge for each siRNAs at 0hr (dashed box plots) and 10hr (empty box plots) of migration.
442 Number of cells counted for siCT, blue, n = 123 0hr, n =126 10hr; for siCT/CK666 treated cells,
443 orange, n =165 0hr, n =152 10hr; for siARP2/3 n=114 at 0hr, n =120 at 10hr. H) Time evolution
444 of monolayer expansion (shown as the distance covered by the cell monolayer from the initial
445 point). Number of monolayers for siCT blue, n =3; siCT/CK666, orange, n =3; siARP2/3, gray,
446 n=3.

447 **Fig. 4: Downregulation of the CRB3 complex and ARP2/3 alter the organization of the F-**
448 **actin.** A-C') Representative images showing the effect of each siRNA on the organization of
449 the F-actin at the basal domain (siCT (A, A'), siCRB3 (B, B'), siARP2/3 (C, C' (at 0hr and 10hr of
450 migration. Blue arrowheads: F-actin cable, yellow arrowheads: actin arcs, red dash line:
451 outline for the basal edge. Scale bars= 15 μ m. D-F') Representation Orientation maps of actin
452 fibers (siCT (D,D'), siCRB3 (E,E') and siARP2/3 (F,F')). Scale bar in degree. Insets are
453 representative zoomed regions of actin orientation. G) Quantification of actin fibers
454 orientation area for each siRNAs at 0hr (dashed box plots) and 10hr (empty box plots) of
455 migration. For each siRNA 10 fields of views were quantified. siCT, blue; siCRB3, red; siARP2/3,
456 grey. Data are presented as mean \pm Min Max. H) Quantification of actin fibers coherency for
457 each siRNAs at 0hr (dashed box plots) and 10hr (empty box plots) of migration. For each siRNA
458 10 fields of views were quantified. siCT, blue; siCRB3, red; siARP2/3, grey. Data are presented
459 as mean \pm Min Max.

460

461 **Fig. 5: Downregulation of the CRB3 and ARP2/3 alters the organization of the focal contacts.**
462 Representative images of focal adhesions immunostained with paxillin (top) and paxillin/F-
463 actin (bottom) for siCT(A) , siCRB3 (B), siARP2/3 (C), at 0hr and siCT (A'), siCRB3 (B'), Arp2/3
464 (C') at 10hr.. Scale bars 10 μ m. Representative maps of the Delaunay Triangulation of paxillin
465 for siCT (D), siCRB3 (E), siARP2/3 (F) at 0hr and siCT (D'), siCRB3 (E'), siARP2/3 (F') at 10hr.
466 Scale Bar 10 μ m. G) Quantification of the major length of the focal contacts is represented as
467 dashed box plots (0hr) and empty box plot (10hr). Data are represented as mean \pm Min Max.
468 H) Quantification of the orientation of the focal contacts is represented as dashed box plots
469 (0hr) and empty box plot (10hr). Data are represented as mean \pm Min Max. The total number
470 of focal contacts quantified for siCT, blue, n = 2530, 6 fields of view, 0hr, n= 6652, 15 fields of
471 view, 10hr; siCRB3, red, n=2230, 4 fields of view, 0hr, n=7410, 17 fields, 10hr; siARP2/3, grey,
472 n=1476, 4 fields of view, 0hr, n =5806, 13 fields of view, 10hr. Data are presented as mean \pm
473 Min Max. I) Quantification of the area of the triangle obtained by a Delaunay triangulation
474 over all the focal contacts for each siRNA condition at 0hr (dashed boxplot) and at 10hr (empty
475 boxplot). The box plots represent the mean \pm Min Max of all the triangles measured for each
476 siRNAs. siCT, blue, n=23232, 7 fields of view, 0hr, n= 25140, 16 fields of view, 10hr; siCRB3,
477 red, n= 12917, 4 fields of view, 0hr, n=37164, 18 fields of view, 10hr, siARP2/3, grey, n= 11737,
478 n=4, 0hr, n= 13816, 6 fields of view, 10hr .

479 **Fig. 6: Downregulation of the CRB3 complex and Arp2/3 alters monolayers physical**
480 **properties.** Representative maps showing the effect of each siRNAs on monolayers dynamics
481 at 0hr and 10hr of migration. Representative phase contrast images of siCT (A), siCRB3 (B),
482 siArp2/3 (C) at 0hr and siCT (A'), siCR3 (B'), siArp2/3 (C') at 10hr . Representative traction force
483 maps for siCT (D), siCRB3 (E), siARP2/3 (F) at 0hr and siCT (D'), siCRB3 (E'), siARP2/3 (F') at
484 10hr. Representative intercellular tension maps σ_{xx} , or siCT (G), siCRB3 (H), siARP2/3 (I) at 0hr
485 and siCT (G'), siCRB3 (H'), siARP2/3 (I') at 10hr. Representative vectorial fields of intercellular
486 tension for siCT (J), siCRB3 (K), siARP2/3 (L) at 0hr and siCT (J'), siCRB3 (K'), siARP2/3 (L') at
487 10hr.. Scale bars= 100 μ m. M-O) Time evolution of traction forces (M)intercellular tension (N),
488 tension entropy (O) for the siCT (blue), siCRB3 (red), siARP2/3 (grey). Data are presented as
489 mean \pm SEM. siCT n=7 independent cell monolayers, siCRB3 n=3 independent cell monolayers,
490 siARP2/3, n = 3 independent monolayers.

491

492 **Fig. 7: The depleted cells exhibit different mechanical properties before showing difference**
493 **at the biological level.** Effect of siRNAs on biological and physical properties expressed in z-
494 scores at 0hr (A, B) and at 10hr of migration (C, D). OI: Orientation Index, La : number of
495 lamellipodia, EF : Elongation Factor; Disp :Dispersion, Cohe : Coherency, V : velocity, Tnr :
496 normal Traction, Sxx : Normal component of the stress tensor in the x direction , Shr : Shear
497 component of the stress tensor, Ent: Entropy.

498

499 References

- 500 1. Rvasio, A. *et al.* Regulation of epithelial cell organization by tuning cell–substrate adhesion.
501 *Integr. Biol.* **7**, 1228–1241 (2015).
- 502 2. Ojakian, G. K. & Schwimmer, R. Regulation of epithelial cell surface polarity reversal by beta 1
503 integrins. *J Cell Sci* **107 (Pt 3)**, 561–576 (1994).
- 504 3. Wang, A. Z., Ojakian, G. K. & Nelson, W. J. Steps in the morphogenesis of a polarized epithelium.
505 II. Disassembly and assembly of plasma membrane domains during reversal of epithelial cell
506 polarity in multicellular epithelial (MDCK) cysts. *J Cell Sci* **95 (Pt 1)**, 153–165 (1990).
- 507 4. Dongre, A. & Weinberg, R. A. New insights into the mechanisms of epithelial–mesenchymal
508 transition and implications for cancer. *Nat Rev Mol Cell Biol* **20**, 69–84 (2019).
- 509 5. Friedl, P., Locker, J., Sahai, E. & Segall, J. E. Classifying collective cancer cell invasion. *Nat Cell Biol*
510 **14**, 777–783 (2012).
- 511 6. Krndija, D. *et al.* Active cell migration is critical for steady-state epithelial turnover in the gut.
512 *Science* **365**, 705–710 (2019).
- 513 7. Lecaudey, V. & Gilmour, D. Organizing moving groups during morphogenesis. *Current Opinion in*
514 *Cell Biology* **18**, 102–107 (2006).
- 515 8. Yang, J. *et al.* Guidelines and definitions for research on epithelial–mesenchymal transition. *Nat*
516 *Rev Mol Cell Biol* **21**, 341–352 (2020).
- 517 9. Pérez-González, C. *et al.* Active wetting of epithelial tissues. *Nat Phys* **15**, 79–88 (2019).
- 518 10. Poujade, M. *et al.* Collective migration of an epithelial monolayer in response to a model wound.
519 *PNAS* **104**, 15988–15993 (2007).
- 520 11. Avizienyte, E., Fincham, V. J., Brunton, V. G. & Frame, M. C. Src SH3/2 domain-mediated peripheral
521 accumulation of Src and phospho-myosin is linked to deregulation of E-cadherin and the epithelial-
522 mesenchymal transition. *Mol Biol Cell* **15**, 2794–2803 (2004).

- 523 12. Collins, C. & Nelson, W. J. Running with Neighbors: Coordinating Cell Migration and Cell-Cell
524 Adhesion. *Curr Opin Cell Biol* **36**, 62–70 (2015).
- 525 13. Goodwin, K. *et al.* Cell–cell and cell–extracellular matrix adhesions cooperate to organize
526 actomyosin networks and maintain force transmission during dorsal closure. *MBoC* **28**, 1301–1310
527 (2017).
- 528 14. Haynes, J., Srivastava, J., Madson, N., Wittmann, T. & Barber, D. L. Dynamic actin remodeling
529 during epithelial–mesenchymal transition depends on increased moesin expression. *MBoC* **22**,
530 4750–4764 (2011).
- 531 15. Le Borgne-Rochet, M. *et al.* P-cadherin-induced decorin secretion is required for collagen fiber
532 alignment and directional collective cell migration. *Journal of Cell Science* jcs.233189 (2019)
533 doi:10.1242/jcs.233189.
- 534 16. Maruthamuthu, V., Aratyn-Schaus, Y. & Gardel, M. L. Conserved F-actin Dynamics and Force
535 Transmission at Cell Adhesions. *Curr Opin Cell Biol* **22**, 583–588 (2010).
- 536 17. Monier-Gavelle, F. & Duband, J.-L. Cross Talk between Adhesion Molecules: Control of N-cadherin
537 Activity by Intracellular Signals Elicited by $\beta 1$ and $\beta 3$ Integrins in Migrating Neural Crest Cells.
538 *Journal of Cell Biology* **137**, 1663–1681 (1997).
- 539 18. Das, T. *et al.* A molecular mechanotransduction pathway regulates collective migration of
540 epithelial cells. *Nat Cell Biol* **17**, 276–287 (2015).
- 541 19. Vishwakarma, M. *et al.* Mechanical interactions among followers determine the emergence of
542 leaders in migrating epithelial cell collectives. *Nat Commun* **9**, 3469 (2018).
- 543 20. Tambe, D. T. *et al.* Collective cell guidance by cooperative intercellular forces. *Nature Mater* **10**,
544 469–475 (2011).
- 545 21. Trepatt, X. *et al.* Physical forces during collective cell migration. *Nature Phys* **5**, 426–430 (2009).
- 546 22. Zaritsky, A. *et al.* Seeds of Locally Aligned Motion and Stress Coordinate a Collective Cell Migration.
547 *Biophys J* **109**, 2492–2500 (2015).
- 548 23. Bazellieres, E. *et al.* Control of cell–cell forces and collective cell dynamics by the intercellular
549 adhesome. *Nat Cell Biol* **17**, 409–420 (2015).
- 550 24. Elosegui-Artola, A. *et al.* Rigidity sensing and adaptation through regulation of integrin types.
551 *Nature Mater* **13**, 631–637 (2014).
- 552 25. Mertz, A. F. *et al.* Cadherin-based intercellular adhesions organize epithelial cell–matrix traction
553 forces. *Proc Natl Acad Sci U S A* **110**, 842–847 (2013).
- 554 26. Plutoni, C. *et al.* P-cadherin promotes collective cell migration via a Cdc42-mediated increase in
555 mechanical forces. *Journal of Cell Biology* **212**, 199–217 (2016).
- 556 27. Roca-Cusachs, P. *et al.* Integrin-dependent force transmission to the extracellular matrix by -
557 actinin triggers adhesion maturation. *Proceedings of the National Academy of Sciences* **110**,
558 E1361–E1370 (2013).
- 559 28. DeMali, K. A., Sun, X. & Bui, G. A. Force Transmission at Cell–Cell and Cell–Matrix Adhesions.
560 *Biochemistry* **53**, 7706–7717 (2014).
- 561 29. Bazellieres, E., Aksenova, V., Barthélémy-Requin, M., Massey-Harroche, D. & Le Bivic, A. Role of
562 the Crumbs proteins in ciliogenesis, cell migration and actin organization. *Seminars in Cell &*
563 *Developmental Biology* **81**, 13–20 (2018).
- 564 30. De Pascalis, C. & Etienne-Manneville, S. Single and collective cell migration: the mechanics of
565 adhesions. *Mol Biol Cell* **28**, 1833–1846 (2017).
- 566 31. Goodwin, K. *et al.* Cell–cell and cell–extracellular matrix adhesions cooperate to organize
567 actomyosin networks and maintain force transmission during dorsal closure. *MBoC* **28**, 1301–1310
568 (2017).
- 569 32. Lemmers, C. *et al.* CRB3 Binds Directly to Par6 and Regulates the Morphogenesis of the Tight
570 Junctions in Mammalian Epithelial Cells. *Mol Biol Cell* **15**, 1324–1333 (2004).
- 571 33. Shin, K., Wang, Q. & Margolis, B. PATJ regulates directional migration of mammalian epithelial
572 cells. *EMBO Rep* **8**, 158–164 (2007).

- 573 34. Tepass, U., Theres, C. & Knust, E. crumbs encodes an EGF-like protein expressed on apical
574 membranes of Drosophila epithelial cells and required for organization of epithelia. *Cell* **61**, 787–
575 799 (1990).
- 576 35. Tepass, U. & Knust, E. crumbs and stardust Act in a Genetic Pathway That Controls the Organization
577 of Epithelia in Drosophila melanogaster. *Developmental Biology* **159**, 311–326 (1993).
- 578 36. Assémat, E. *et al.* The multi-PDZ domain protein-1 (MUPP-1) expression regulates cellular levels of
579 the PALS-1/PATJ polarity complex. *Experimental Cell Research* **319**, 2514–2525 (2013).
- 580 37. Etienne-Manneville, S. Polarity proteins in migration and invasion. *Oncogene* **27**, 6970–6980
581 (2008).
- 582 38. Lüttgenau, S. M. *et al.* Pals1 prevents Rac1-dependent colorectal cancer cell metastasis by
583 inhibiting Arf6. *Molecular Cancer* **20**, 74 (2021).
- 584 39. Iioka, H. *et al.* Crumbs3 is a critical factor that regulates invasion and metastasis of colon
585 adenocarcinoma via the specific interaction with FGFR1. *Int J Cancer* **145**, 2740–2753 (2019).
- 586 40. Iioka, H., Saito, K. & Kondo, E. Crumbs3 regulates the expression of glycosphingolipids on the
587 plasma membrane to promote colon cancer cell migration. *Biochemical and Biophysical Research
588 Communications* **519**, 287–293 (2019).
- 589 41. Karp, C. M. *et al.* Role of the polarity determinant crumbs in suppressing mammalian epithelial
590 tumor progression. *Cancer Res* **68**, 4105–4115 (2008).
- 591 42. Li, P. *et al.* CRB3 downregulation confers breast cancer stem cell traits through TAZ/ β -catenin.
592 *Oncogenesis* **6**, e322–e322 (2017).
- 593 43. Artursson, P. Epithelial transport of drugs in cell culture. I: A model for studying the passive
594 diffusion of drugs over intestinal absorptive (Caco-2) cells. *Journal of Pharmaceutical Sciences* **79**,
595 476–482 (1990).
- 596 44. Bazellieres, E. *et al.* Apico-basal elongation requires a drebrin-E–EB3 complex in columnar human
597 epithelial cells. *Journal of Cell Science* **125**, 919–931 (2012).
- 598 45. Toya, M. *et al.* CAMSAP3 orients the apical-to-basal polarity of microtubule arrays in epithelial
599 cells. *PNAS* **113**, 332–337 (2016).
- 600 46. Basson, M. D., Modlin, I. M. & Madri, J. A. Human enterocyte (Caco-2) migration is modulated in
601 vitro by extracellular matrix composition and epidermal growth factor. *J. Clin. Invest.* **90**, 15–23
602 (1992).
- 603 47. Koch, S. *et al.* Dkk-1 Inhibits Intestinal Epithelial Cell Migration by Attenuating Directional
604 Polarization of Leading Edge Cells. *MBoC* **20**, 4816–4825 (2009).
- 605 48. Sanders, M. A. & Basson, M. D. p130cas but Not Paxillin Is Essential for Caco-2 Intestinal Epithelial
606 Cell Spreading and Migration on Collagen IV *. *Journal of Biological Chemistry* **280**, 23516–23522
607 (2005).
- 608 49. Assémat, E., Bazellieres, E., Pallesi-Pocachard, E., Le Bivic, A. & Massey-Harroche, D. Polarity
609 complex proteins. *Biochim Biophys Acta* **1778**, 614–630 (2008).
- 610 50. Schaks, M., Giannone, G. & Rottner, K. Actin dynamics in cell migration. *Essays Biochem* **63**, 483–
611 495 (2019).
- 612 51. Zegers, M. M. & Friedl, P. Rho GTPases in collective cell migration. *Small GTPases* **5**, e28997 (2014).
- 613 52. Di Nardo, A. *et al.* Arp2/3 complex-deficient mouse fibroblasts are viable and have normal leading-
614 edge actin structure and function. *Proc Natl Acad Sci U S A* **102**, 16263–16268 (2005).
- 615 53. Ilatovskaya, D. V. *et al.* Arp2/3 complex inhibitors adversely affect actin cytoskeleton remodeling
616 in the cultured murine kidney collecting duct M-1 cells. *Cell Tissue Res* **354**, 10.1007/s00441-013-
617 1710-y (2013).
- 618 54. Gao, Y., Lui, W., Lee, W. M. & Cheng, C. Y. Polarity protein Crumbs homolog-3 (CRB3) regulates
619 ectoplasmic specialization dynamics through its action on F-actin organization in Sertoli cells. *Sci
620 Rep* **6**, 28589 (2016).
- 621 55. Qin, S., Ricotta, V., Simon, M., Clark, R. A. F. & Rafailovich, M. H. Continual Cell Deformation
622 Induced via Attachment to Oriented Fibers Enhances Fibroblast Cell Migration. *PLOS ONE* **10**,
623 e0119094 (2015).

- 624 56. Massou, S. *et al.* Cell stretching is amplified by active actin remodelling to deform and recruit
625 proteins in mechanosensitive structures. *Nat Cell Biol* **22**, 1011–1023 (2020).
- 626 57. Bachir, A. I., Horwitz, A. R., Nelson, W. J. & Bianchini, J. M. Actin-Based Adhesion Modules Mediate
627 Cell Interactions with the Extracellular Matrix and Neighboring Cells. *Cold Spring Harb Perspect*
628 *Biol* **9**, a023234 (2017).
- 629 58. Choi, C. K. *et al.* Actin and α -actinin orchestrate the assembly and maturation of nascent adhesions
630 in a myosin II motor-independent manner. *Nat Cell Biol* **10**, 1039–1050 (2008).
- 631 59. Parsons, J. T., Horwitz, A. R. & Schwartz, M. A. Cell adhesion: integrating cytoskeletal dynamics and
632 cellular tension. *Nat Rev Mol Cell Biol* **11**, 633–643 (2010).
- 633 60. Lecuit, T., Lenne, P.-F. & Munro, E. Force generation, transmission, and integration during cell and
634 tissue morphogenesis. *Annu Rev Cell Dev Biol* **27**, 157–184 (2011).
- 635 61. Fogg, V. C., Liu, C.-J. & Margolis, B. Multiple regions of Crumbs3 are required for tight junction
636 formation in MCF10A cells. *Journal of Cell Science* **118**, 2859–2869 (2005).
- 637 62. Lin, W.-H., Asmann, Y. W. & Anastasiadis, P. Z. Expression of Polarity Genes in Human Cancer.
638 *Cancer Inform* **14**, 15–28 (2015).
- 639 63. Mao, X. *et al.* CRB3 regulates contact inhibition by activating the Hippo pathway in mammary
640 epithelial cells. *Cell Death Dis* **8**, e2546–e2546 (2018).
- 641 64. Stucke, V. M., Timmerman, E., Vandekerckhove, J., Gevaert, K. & Hall, A. The MAGUK Protein MPP7
642 Binds to the Polarity Protein hDlg1 and Facilitates Epithelial Tight Junction Formation. *MBoC* **18**,
643 1744–1755 (2007).
- 644 65. Li, P. *et al.* Crumbs protein homolog 3 (CRB3) expression is associated with oestrogen and
645 progesterone receptor positivity in breast cancer. *Clin Exp Pharmacol Physiol* **46**, 837–844 (2019).
- 646 66. Sidor, C., Stevens, T. J., Jin, L., Boulanger, J. & Röper, K. Rho-Kinase Planar Polarization at Tissue
647 Boundaries Depends on Phospho-regulation of Membrane Residence Time. *Dev Cell* **52**, 364-
648 378.e7 (2020).
- 649 67. Pollard, T. D. & Cooper, J. A. Actin, a Central Player in Cell Shape and Movement. *Science* **326**,
650 1208–1212 (2009).
- 651 68. Massey, D. & Maroux, S. The carbohydrate moiety of aminopeptidase N of rabbit intestinal brush-
652 border membrane. *FEBS Letters* **181**, 207–210 (1985).

653
654

655

656 **Supplementary Figures**

657

658 **Fig. Supplementary 1: Protein expression levels after siRNA transfections.** A-B) Immunoblot
659 analysis showing the expression of PATJ, PALS1, CRB3 and Arp2/3, 5 days after transfections
660 with siCT, siCRB3, siPATJ, siPALS1 and siARP2/3. α -Tubulin was used to standardize the loading
661 conditions between the different depletions. C) Quantification of protein expression levels
662 normalized to siCT cells. Data are represented as mean \pm SEM. For each protein, n=3 samples
663 pooled from 3 independent transfections.

664

665 **Fig. Supplementary 2: CRB3 interacts with ARP2/3** A) Scheme of CRB3 full length (CRB3 FL),
666 cytoplasmic domain of CRB3 (CRB3 cyt) and the FERM binding domain of CRB3 that are used
667 as peptide bait for the peptide pull-down. B) siCT lysates were pulled-down with the 3

668 peptides (CRB3 FL, CRB3 cyt and CRB3 FERMBD), and probed to detect PALS1 and ARP2/3
669 expression.

670

671 **Fig. Supplementary 3: Downregulation of the CRB3 complex and ARP2/3 alter the**
672 **organization of the F-actin.** A-I') Representative images showing the effect of each siRNA on
673 the organization of the F-actin at the apical domain: siCT (A, A'), siCRB3 (B, B'), siARP2/3 (C,
674 C'); at the lateral domain siCT (D, D'), siCRB3 (E, E'), siARP2/3 (F, F'), and in xz section siCT (G,
675 G'), siCRB3 (H, H') and siARP2/3 (I, I') at 0hr and 10hr of migration. Red dash line: outline for
676 the basal edge, red asterisk: microvilli. Scale bars= 15 μ m. J-K) Quantification of cell spreading
677 (J) and deformations (K) for each siRNAs at 0hr (dashed box plots) and 10hr (empty box plots)
678 of migration. siCT, blue, n = 4 monolayers; siCRB3, red, n= 4 monolayers; siARP2/3 , gray, n=4
679 monolayers. Data are presented as mean \pm SEM. L-M) Monolayer height as function of the
680 distance from the center of the cell monolayer at 0hr (L) and 10hr (M). For the different time
681 points several lateral views were measured for each siRNAs (0hr, n=44, 10hr, n= 44, siCT, blue;
682 siCRB3, red; siARP2/3 , gray. Data are presented as mean \pm SEM.

683

684 **Fig. Supplementary 4: Downregulation of the CRB3 complex and ARP2/3 alter the**
685 **organization of the focal adhesions.** A-F') Representative images showing the effect of each
686 siRNA on the organization of the focal adhesion and the respective segmentation map: siCT
687 (A, A'), siCRB3 (B, B'), siARP2/3 (C, C') at 0hr and siCT (D, D'), siCRB3 (E, E') and siARP2/3 (F,
688 F') at 10hr. G) Proportion of focal contacts as function of their sizes. The box plots represented
689 the ratio between the number of focal contacts categorized by their sizes (0.25 μ m: brown,
690 0.5 μ m: green and >1 μ m: blue) to the total number of focal contacts at 0hr (dashed boxplot)
691 and 10hr (empty box plot). The total number of focal contacts quantified for siCT, blue, n =
692 2530, 6 fields of view, 0hr, n= 6652, 15 fields of view, 10hr; siCRB3, red, n=2230, 4 fields of
693 view, 0hr,n=7410, 17 fields, 10hr; siARP2/3, grey, n=1476, 4 fields of view, 0hr, n =5806, 13
694 fields of view, 10hr. Data are presented as mean \pm Min Max.

695

696

697 **Material and Methods**

698 **Caco2 cell line culture, transfection and drug treatment**

699 Caco2 cells were grown on DMEM-glutamax media supplemented with 20% Foetal Bovine
700 Serum, 1% of Non-Essential Amino Acid, 100U/mL Penicillin,Streptomycin.

701 siRNA transfections were performed by electroporation using Amaxa technology. 100pmoles
702 of a pool of 3 siRNAs and 1.5 10^6 freshly trypsinized Caco2 cells were transfected using the
703 B24 program following the manufacturer recommendations. Cells were then seeded on a 6-

704 well plates. 4 days after transfections, cells were trypsinized, 50000 cells were seeded on soft
705 polyacrylamide gels and the remaining cells were processed by western blot.

706 The inhibition of branched actin was performed by adding 67 μ M, directly in the cell medium,
707 of CK666 drug directly after the removal of the PDMS membrane.

708 **Preparation of soft polyacrylamide gels**

709 Polyacrylamide gels with a Young's modulus of 12 kPa were prepared as described previously
710 (Bazellieres et al 2015). A solution of 19% acrylamide, 8% bis-acrylamide, 0.5% ammonium
711 persulfate, 0.1% tetramethylethylenediamine, 0.64% of 200nm diameter red fluorescent
712 carboxylate-modified beads and 2mg/mL NH-acrylate was prepared and allowed to
713 polymerize at RT for 1hour. After polymerization, gels were incubated with 0.1mg/mL of
714 collagen I overnight at 4°C.

715 **Fabrication of PDMS membrane**

716 Polydimethylsiloxane (PDMS) membranes were fabricated according to procedures described
717 previously (Bazellieres et al 2015). SU8-50 masters containing rectangles of 300 \times 2,500 μ m
718 were obtained using conventional photolithography. Uncured PDMS was spin-coated on the
719 masters to a thickness lower than the height of the SU8 rectangular feature and cured
720 overnight at 60°C. A thick border of PDMS was left at the edges of the membranes for handling
721 purposes. PDMS was then peeled off from the master and kept in ethanol at 4°C until use.

722 **Epithelial cell monolayer patterning**

723 To pattern the cells on top of the polyacrylamide gels, a PDMS membrane was deposited on
724 top of the polyacrylamide gel and 50000 cells were seeded within the rectangle defined by
725 the PDMS stencil. Cells were allowed to adhere and differentiated on the gel for 24 hours. 15
726 minutes before time lapse imaging, the PDMS membrane was carefully removed allowing the
727 cells to migrate toward the freely available substrate.

728 **Time lapse imaging and monolayer expansion quantification**

729 Multidimensional acquisitions were performed on an automated inverted microscope (Zeiss
730 AxioObserver, 10 \times lens) equipped with thermal, CO₂, and humidity control, using Zen
731 software. Images were obtained every 10 minutes during 600 minutes. 6 independent
732 monolayers were imaged in parallel using a motorized XY stage.

733 Based on the phase contrast images, a segmented imaged of the edges of the monolayer was
734 created at each time frame. The Euclidean distance between the two edges, at each pixel, for
735 each siRNA was analyzed using a custom written MatLab codes based on the bwdist function.

736 **Immunoprecipitation and western blotting**

737 For protein expression level confluent caco2 cells were lysed in lysis buffer (50 mM Tris HCL
738 pH 7.4, 150 mM NaCl, 0.5% NP40) with protease inhibitor cocktail containing 1 μ g/ml antipain,

739 1 µg/ml pepstatin, 15 µg/ml benzamidine, and 1 µg/ml leupeptin. Lysates were cleared by
740 centrifugation at 20000g for 30min at 4°C. Protein expression levels were measured using
741 Western Blot. Cell lysates were then mixed with Laemmli 1X and heated at 95°C for 5 minutes.
742 Next, cell lysates were loaded to NuPAGE 4-12% Bis-Tris gel (ThermoFisher Scientific,
743 Courtaboeuf, France) for electrophoresis. Proteins were then transferred to a nitrocellulose
744 membrane (Whatman, GE Healthcare Life Sciences), which was blocked with 5% dry-milk-Tris
745 Buffer saline, 0.2% Tween, and incubated with primary antibodies (overnight at 4°C) followed
746 by the horseradish peroxidase coupled secondary antibodies (1h, room temperature). Bands
747 were revealed using chemi-luminescence reagent plus (Perkin Elmer) and visualized by MyECL
748 imager (ThermoFisher Scientific, Courtaboeuf, France). The intensity of the bands was
749 quantified using ImageJ software. Tubulin was used as an endogenous control for
750 normalization. Protein concentrations are reported relative to the control.

751 A phase separation method was used to quantify the amount of ARP2/3 that is associated at
752 the cell membrane in siCT and siCRB3 conditions. Confluent caco2 cells were lysed in lysis
753 buffer (50 mM Tris HCL pH 7.4, 150 mM NaCl, 2% Triton X-114) with protease inhibitor cocktail
754 containing 1 µg/ml antipain, 1 µg/ml pepstatin, 15 µg/ml benzamidine, and 1 µg/ml leupeptin.
755 Lysates were cleared by centrifugation at 20000g for 30min at 4°C, and the supernatant was
756 brought up to 37°C for 5min allowing to collect the phase that contains the membrane bound
757 proteins⁶⁸. After 4 washes with lysis buffer without Triton-X114, bound proteins were
758 processed by western blotting.

759 CRB3 peptide pull-down assays: 150 µL pelleted streptavidin beads (streptavidin agarose
760 resin, ThermoFisher Scientific, Courtaboeuf, France) were coated with 2mg of a biotinylated
761 peptide mimicking the cytoplasmic part of CRB3A (amino-acids 90 to 120) or with the
762 cytoplasmic part containing the FERM binding domain (amino-acids 90 to 100) called CRB3
763 FERMBD, all synthesized by Covalab (Cambridge, UK). The cell lysates were centrifuged at 20
764 000g during 30 min and the supernatants were incubated with 20 µl of streptavidin beads
765 CRB3cyt or CRB3 FERMBD at 4°C overnight. After 4 washes with lysis buffer, bound proteins
766 were processed by western blotting.

767 **Quantification of activated Rac and Rho**

768 Caco2 cells siCT and siCRB3 were lysed in lysis buffer (50mM Tris pH 7.4, 500mM NaCl, 10mM
769 MgCl₂, 1% Triton X-100, 0.1% SDS, 0.5% Sodium Deoxycolate) with protease inhibitor cocktail
770 containing 1 µg/ml antipain, 1 µg/ml pepstatin, 15 µg/ml benzamidine, and 1 µg/ml leupeptin,
771 for 5min on ice. Cell lysates were centrifugated and the supernatants were incubated with the
772 GST fused to Rhotekin-p21Binding Domain (GST-Rhot-PBD) or PAK-p21Binding Domain (GST-
773 PAK-PBD) at 4°C for 30 minutes. The constructs were kindly provided by Michael Sebbagh,
774 CRCM, Marseille. After 3 washes with lysis buffer, bounds proteins were processed by western
775 blotting.

776 **Immunofluorescence**

777 Caco2 cells were washed with PBS, fixed with 3% paraformaldehyde for 10 minutes and
778 permeabilized in 0.5% triton X-100 for 5 minutes. Cells were blocked in 10% FBS for 1 hour at
779 room temperature before being incubated for 4 hours, room temperature, with primary
780 antibodies. After incubation with the appropriate fluorescence-conjugated secondary
781 antibodies for 1hr at room temperature, cells were washed and mounted in DABCO/Mowiol
782 mounting media. Images were acquired with a Zeiss 510 meta confocal microscope, using a
783 63× Objective with 1.4 NA lens.

784

785

786 **Quantification of actin properties**

787 Images were taken using a Zeiss 510 Meta confocal microscope (Zeiss) and were analyzed as
788 following. Actin orientation and coherency were measured using the OrientationJ plugin, the
789 vector field to compute the different parameters was extracted using a grid size of 30 pixels
790 and an α value of 2 pixels. The orientation was defined as the orientation index such as $OI = \cos$
791 (Θ) , Θ defining the angle between the axis of the actin fiber and the direction of migration.

792

793 **Quantification of cell and focal adhesion properties**

794 Images were taken using a Zeiss 510 Meta confocal microscope (Zeiss) and were analyzed as
795 following. Cell contours were detected using cortical actin fluorescent signals, monolayer
796 heights were detected using Z confocal section using actin staining and focal contact were
797 detected using paxillin fluorescent signals in the immunostaining images. Using custom
798 written Matlab codes based on the regionprops function, all the cell contours, monolayer
799 heights and focal contacts within an image were automatically segmented and localized.

800 Based on the segmented images obtained for the cell contours and focal contacts, an ellipse
801 was fitted on each feature and different parameters were extracted such as ellipse area,
802 length of the major and minor axis. The ellipse orientation was defined as the orientation
803 index such as $OI = \cos(\Theta)$, Θ defining the angle between the major axis and the direction of
804 migration.

805 Based on the segmented images obtained for the monolayer height, the Euclidean distance
806 between the two edges, at each pixel, for each siRNA was analyzed using a custom written
807 MatLab codes based on the bwdist function.

808 **Quantification of focal adhesion dispersion**

809 The centroid of each focal contact was automatically determined from the segmented images
810 obtained previously with custom written Matlab scripts. XY position of all centroids were used
811 to build triangles between the nearest neighbors with the Delaunay Triangulation Matlab

812 script. Once the triangulation was obtained, the areas of the triangles were calculated in
813 Matlab.

814 **Traction Force Microscopy**

815 Traction forces were computed using Fourier Transform Traction Microscopy with finite gel
816 thickness. Briefly, as cells migrate, they exert force on the underlying the substrate. Gel
817 deformations are observed by imaging the fluorescent beads embedded within the gels. Gel
818 displacements between any experimental time point and a reference image obtained after
819 cell trypsinization were computed using particle imaging velocimetry software. To reduce
820 systematic biases in subpixel resolution and peak-locking effects, we implemented an iterative
821 process (up to four iterations) based on a continuous window shift technique (Serra-Picamal
822 et al., 2012). Traction vectors $T_{i,j}(t)$ within the field of interest are obtained from displacement
823 vectors $u_{i,j}(t)$ for all time points $t = 1, \dots, n$ and locations (i,j) of the $M \times N$ gel interface matrix.

824 **Monolayer Stress Microscopy**

825 Maps of inter- and intracellular tension within the monolayer were computed using
826 monolayer stress microscopy. In a 2D approximation, monolayer stress is fully captured by a
827 tensor possessing two independent normal components (σ_{xx} and σ_{yy}) and two identical shear
828 components (σ_{xy} and σ_{yx}). At every pixel of the monolayer, these four components of the
829 stress tensor define two particular directions of the plane, one in which the normal stress is
830 maximum and one in which it is minimum. These directions, which are mutually orthogonal,
831 are called principal stress orientations, and the stress values in each principal orientation are
832 called maximum (σ_{11}) and minimum (σ_{22}) stress components. The average normal stress is
833 defined as $\sigma_n = (\sigma_{11} + \sigma_{22})/2$. The spatial resolution and force precision of MSM are formally
834 set by those in the original traction maps.

835

836 **Shannon Entropy Analysis**

837 To apply Shannon's entropy, we partition the range of the angle represented as the angle
838 between two dimensional vectors, into 30° angle bins histogram. With this histogram, the
839 probability of angles in each bin can be calculated, and the information content can be
840 computed using Shannon's entropy as

$$841 \quad H(X) = - \sum_{x_i \in X} p(x_i) \log_2 p(x_i)$$

842

843 The Shannon's entropy allows to measure and thus compare the amount of variation in angle
844 between the vectors in siCT, siCrb3 and siARP2/3 conditions. When the angles between the
845 vectors are different (less aligned) the number of information is high (1), whereas an
846 alignment of the vectors tends to have a more deterministic number of information (0).

847 **Computation of z-scores**

848 The z-score is defined as the signed number of standard deviations an observed quantity
849 deviates from the mean of that quantity. In our study the the z-score of a quantity x (a physical
850 or biological property) in response to a siRNA perturbation is defined as:

$$851 \quad Z = \frac{\bar{x} - \bar{x}_c}{\sigma_c}$$

852 Where \bar{x} is the mean of x under the siRNA perturbation, \bar{x}_c is the mean of x under control
853 conditions, and σ_c is the standard deviation of x under control conditions.

854

855 **siRNAs, Antibodies and reagents**

856 The siRNA sequences used were: siCRB3 (5'-GCAAAUACAGACCACUUCU-3', 5'-
857 CUGCUAUCAUCGUGGUCUU-3', 5'-GUGCGGAAGCUUCGGGAGA-3', 5'-
858 GCUUAAUAGCAGGGAAGAA-3', Dharmacon (On-Target plus Smart Pool)), siCT (5'-
859 CGUACGCGGAAUACUUCGAtt-3', Ambion), siPALS1 (5'-UUCCUUAUGAUGAACUGGcTt-3') and
860 siPATJ (5'-CCAGAUACUCACACUUCAGtt-3', Ambion), siARP2/3 (5'-
861 GGAUUCUUAUGUGCAUCAAtt-3', 5'-GGGAUGAUGAGACCAUGUAtt-3', 5'-
862 AAAUCCUAAUGGAGACAAAtt-3', Ambion)

863 The following primary antibodies were used : rabbit anti CRB3 D2 (Lemmers et al 2004), rat
864 anti CRB3 1E6 (MABT1366 Merck), mouse anti-paxillin (BD transduction 612405), rabbit anti-
865 PATJ Ina2 (Lemmers et al, 2002), chicken anti-PALS1 SN47II (gift from Jan Wijnholds,
866 Kantardzhieva et el, 2005), mouse anti-PALS1 (MPP5, Abnova H00064398), rabbit anti-p34-
867 ARPC2 (07227I, Sigma Aldrich), rabbit anti-pEzrin (Abcam ab47293), mouse anti-Rac (BD
868 transduction, Clone 102), mouse anti-RhoA (SantaCruz 26C2, sc 418). The secondary
869 antibodies used were : Alexa Fluor 488 anti-rat (Invitrogen, A21208), Alexa Fluor 488 anti
870 mouse (Invitrogen, A21202), Alexa Fluor 647 mouse (Jackson Immuno Research 715-605-151)
871 Alexa Fluor 488 anti-rabbit (Invitrogen, A21206), and HRP anti-rat (Jackson Immuno Research
872 712 035 153), HRP anti-mouse (Jackson Immuno Research ,715 035 151), HRP anti-rabbit
873 (Jackson Immuno Research 111 035 003), HRP anti-chicken (Jackson Immuno Research 703
874 035 155). The following probe was used for actin labeling: Phalloidin 647 (Cell Signalling
875 technology, 8940S).

876

877 **Acknowledgments:** We would like to thank Andrea Pasini, Maria Mandela Prunster and
878 Delphine Delacour for discussion. **Funding:** DMH salary is from INSERM, ALB and EB salaries
879 are from CNRS, NG salary is from the Turing Center for Living systems (CenTuri) (ANR-16-
880 CONV-0001).

881 We acknowledge the IBDM imaging facility, member of the national infrastructure France-
882 Biolmaging supported by the French National Research Agency (ANR-10-INBS-04). This work
883 was supported by CNRS and AMU (UMR7288), by the CapoStromex project from the A*MIDEX

884 project (ANR-11-IDEX-0001-02) and the LabEx INFORM (ANR-11-LABX-0054) funded by the
885 “Investissements d’Avenir” French Government program. **Author contributions:** EB conceived
886 the study and designed experiments. EB, DMH, NG performed the experiments, EB and DMH
887 analyzed data. EB developed data analysis tools. VC developed computational mechanical
888 tools. EB and ALB wrote the manuscript. All authors discussed the results and contributed to
889 the manuscript.

890

Figure 2

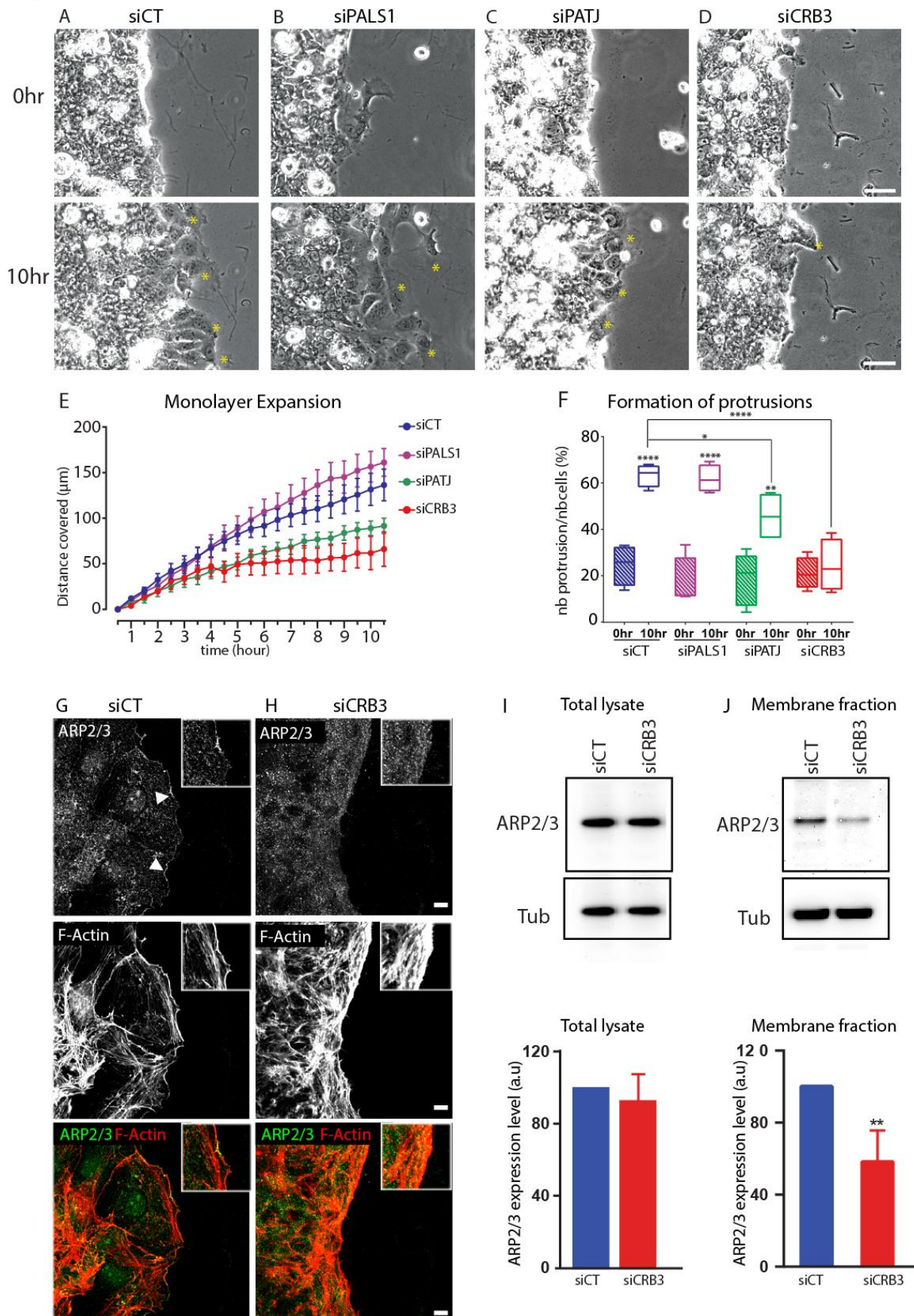


Figure 3

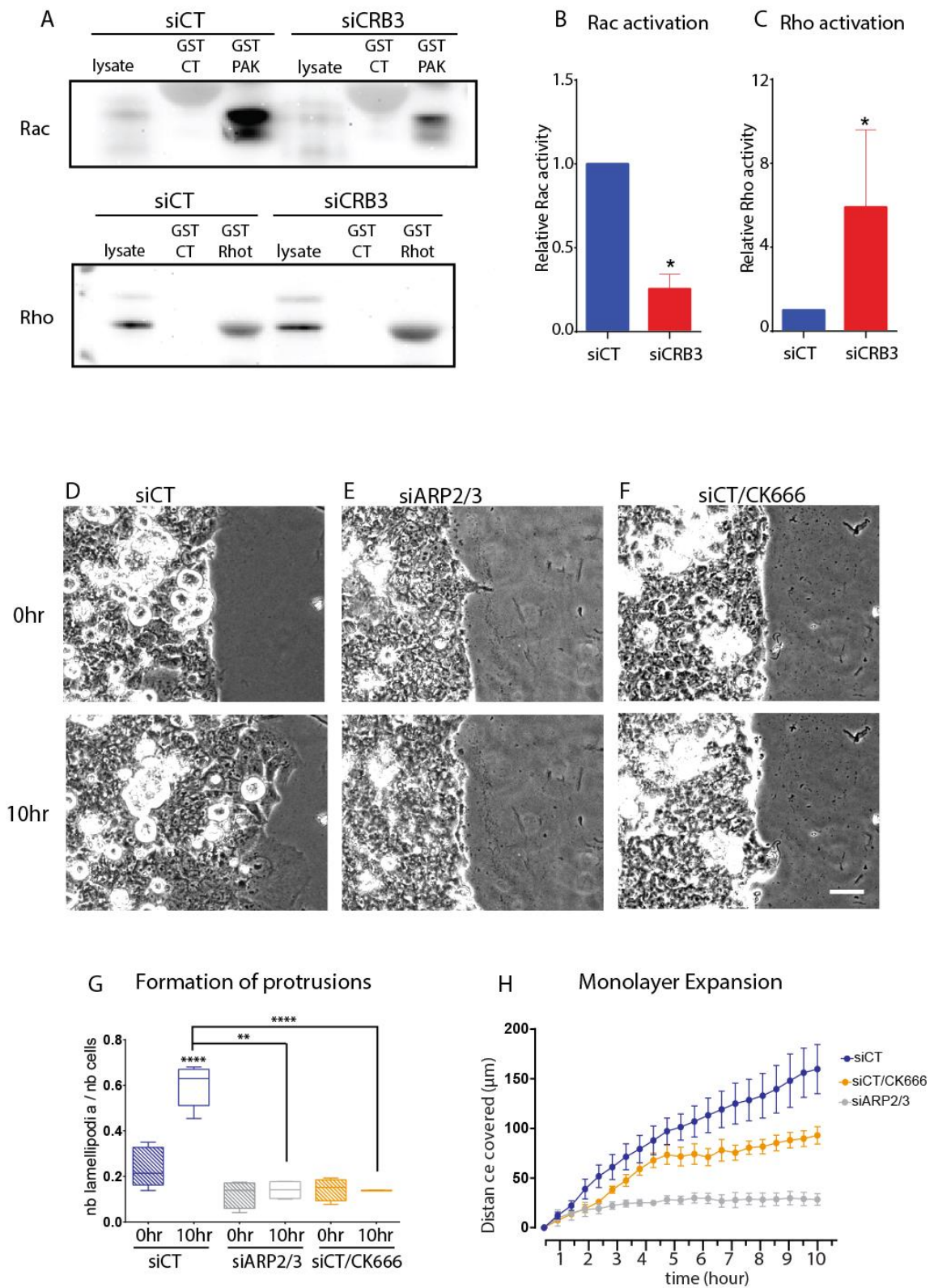


Figure 4

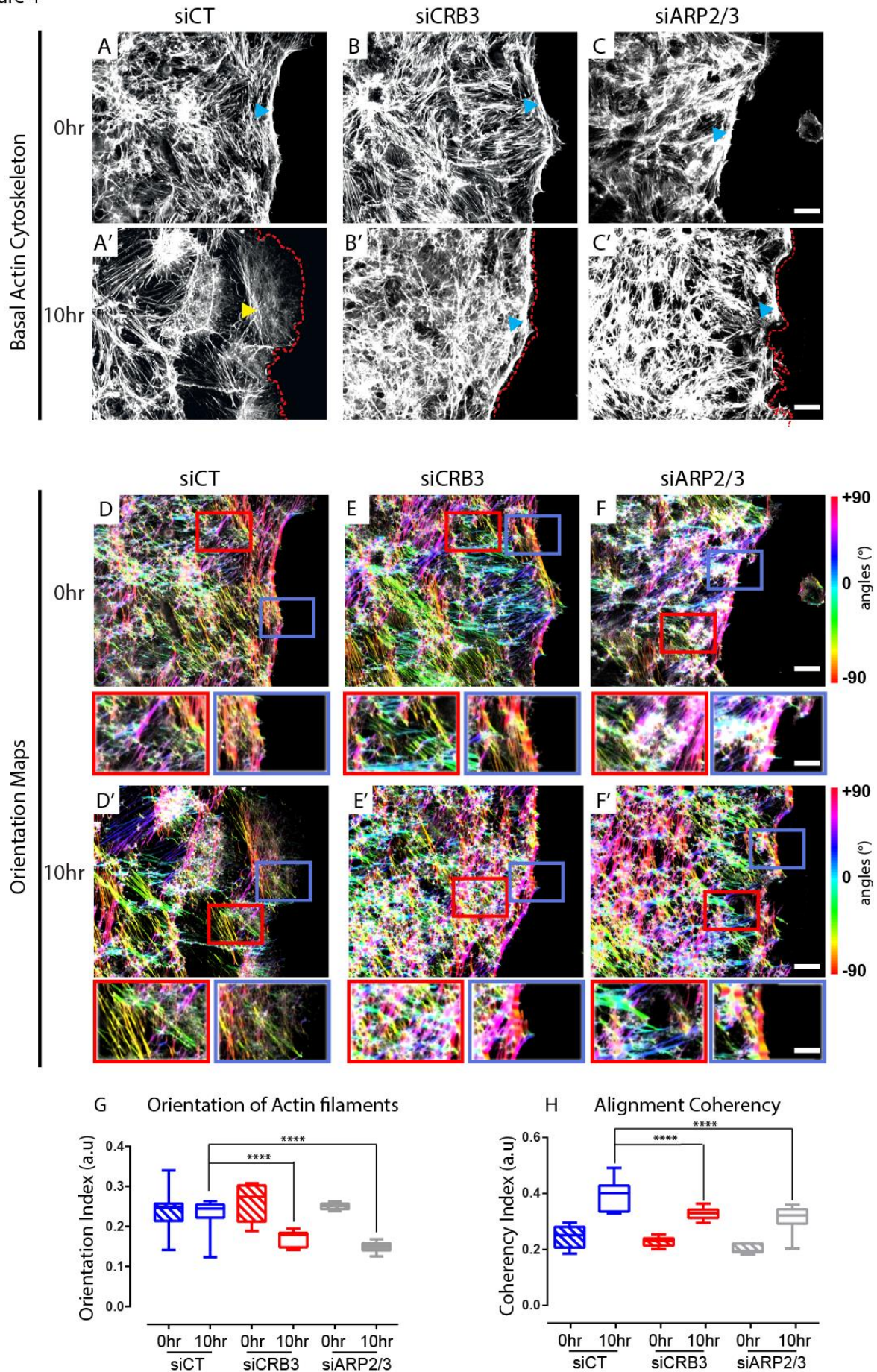


Figure 5

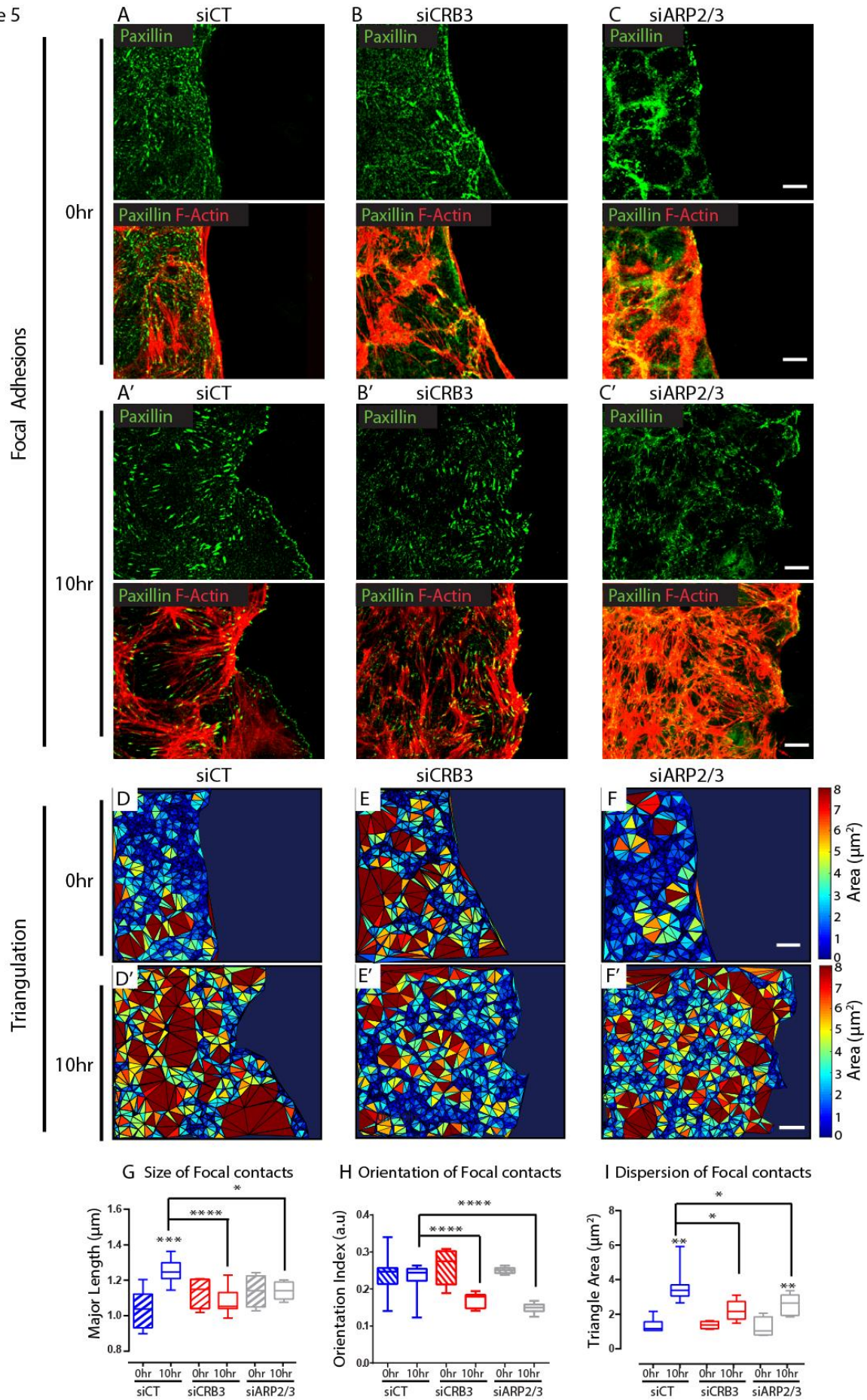


Figure 6

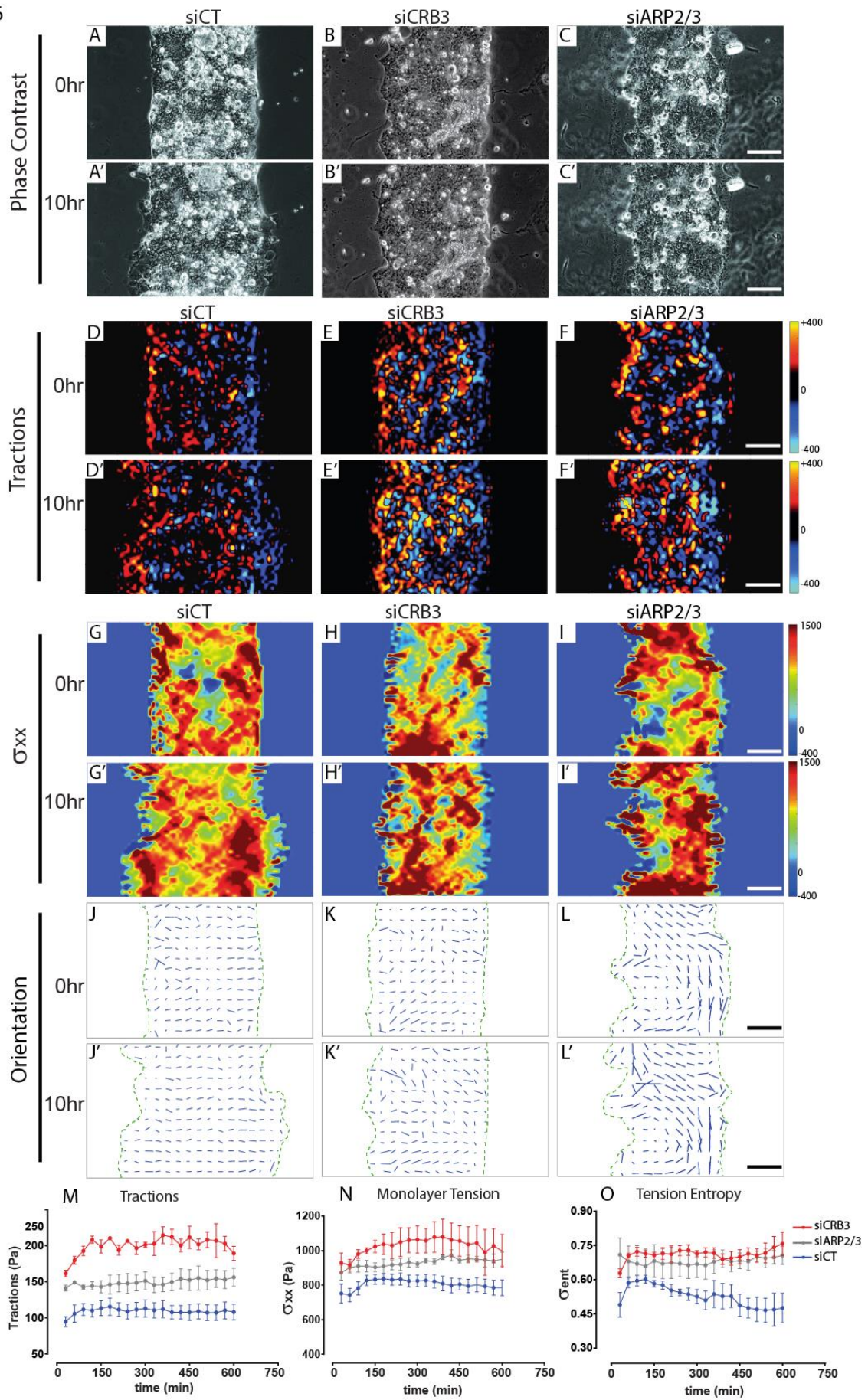


Figure 7

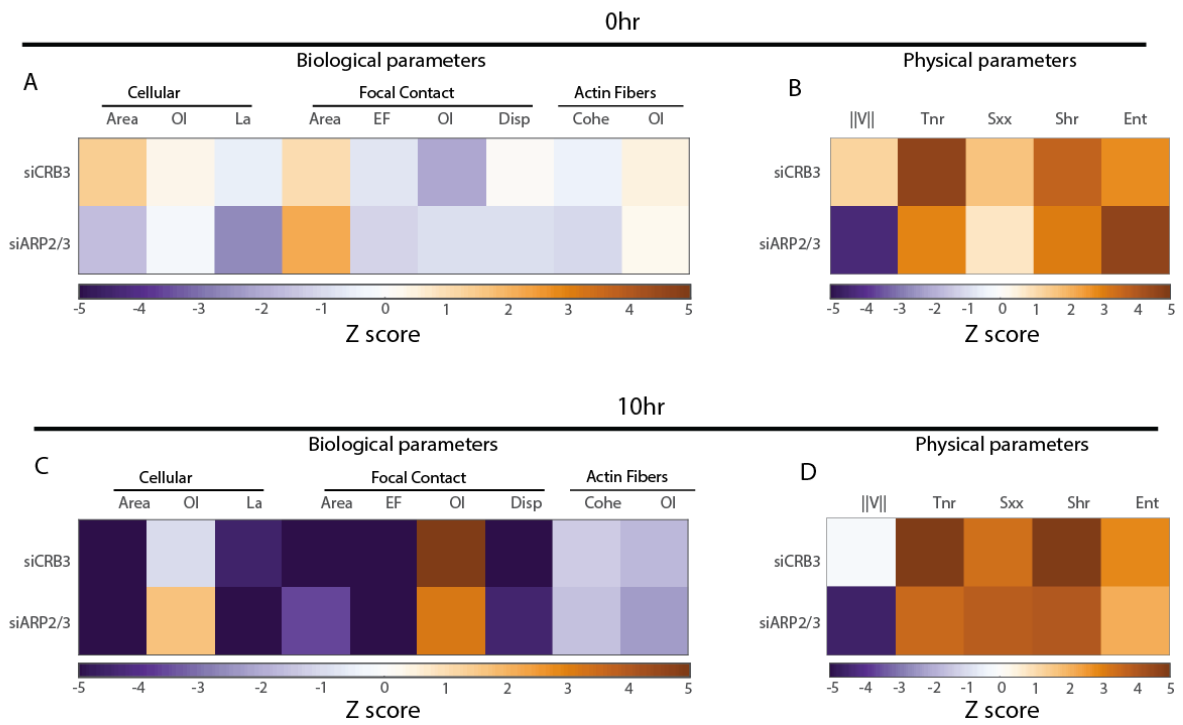


Figure S1

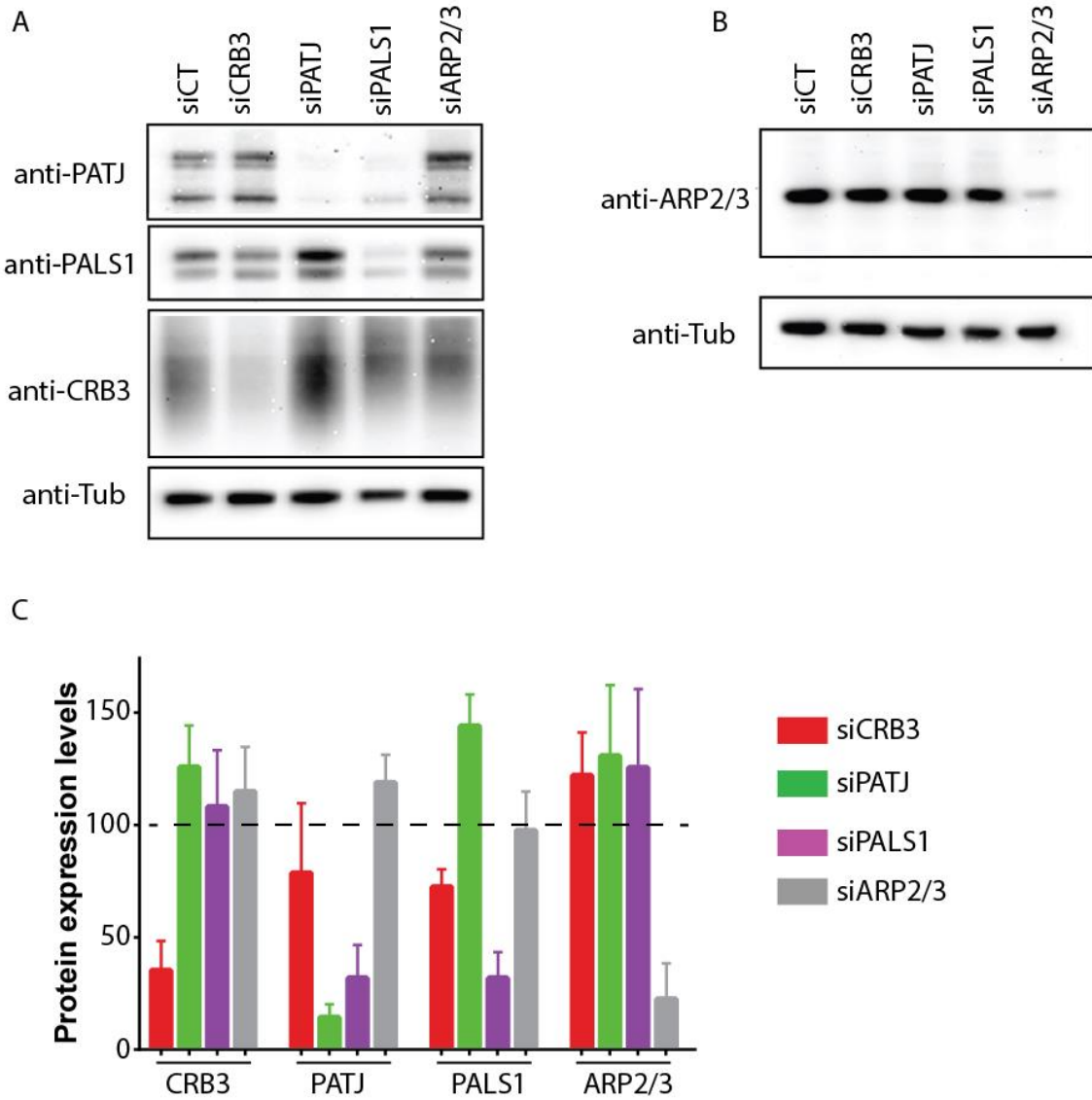


Figure S2

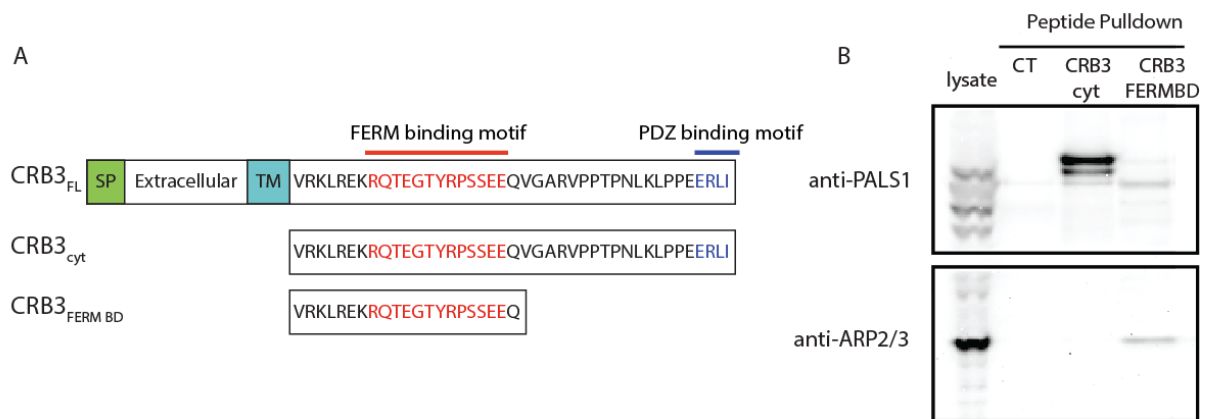
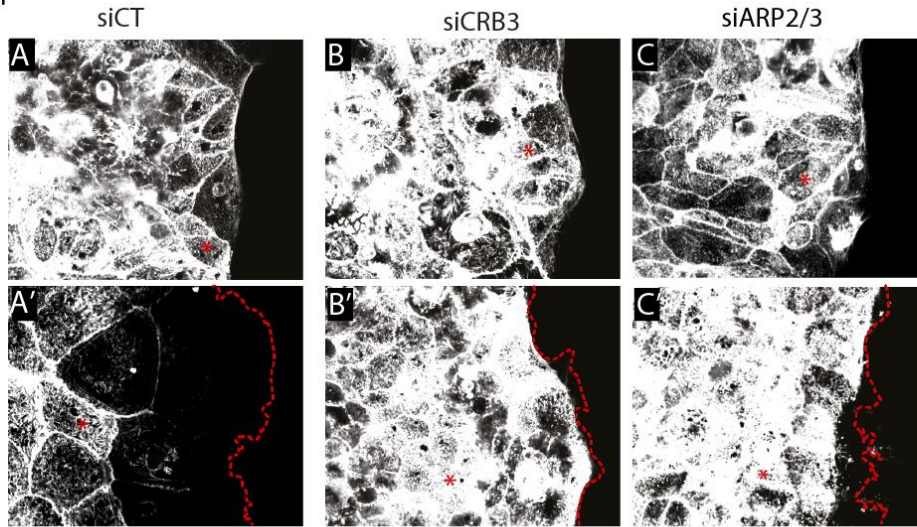
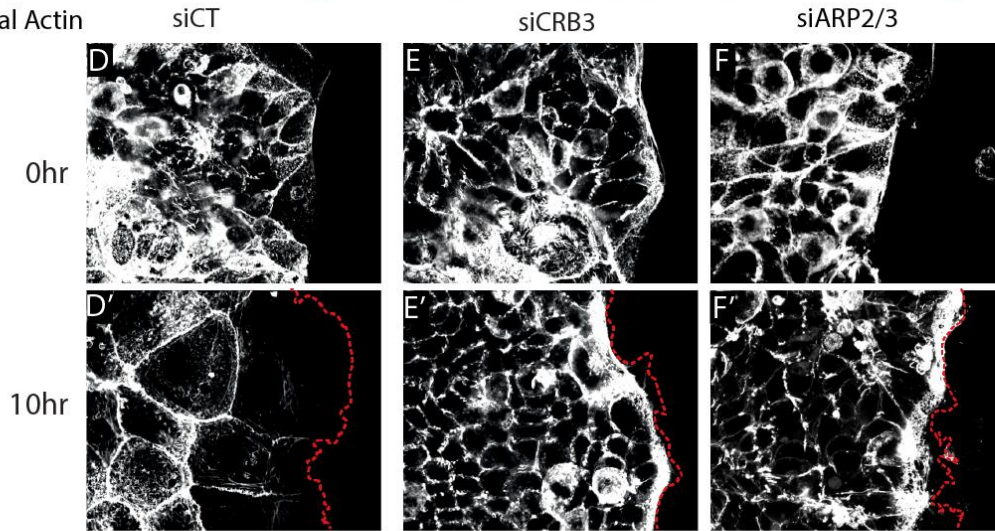


Figure S3

Apical Actin



Lateral Actin



xz section

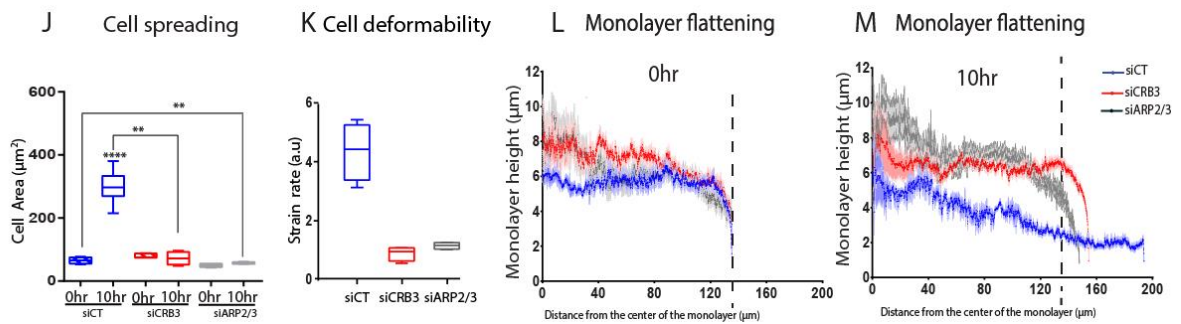
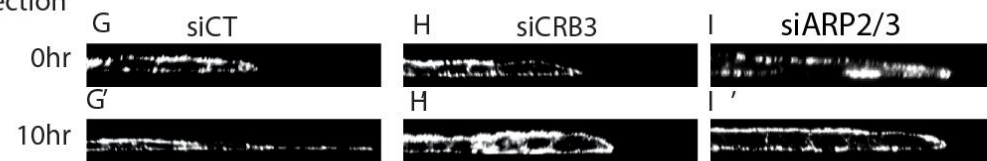
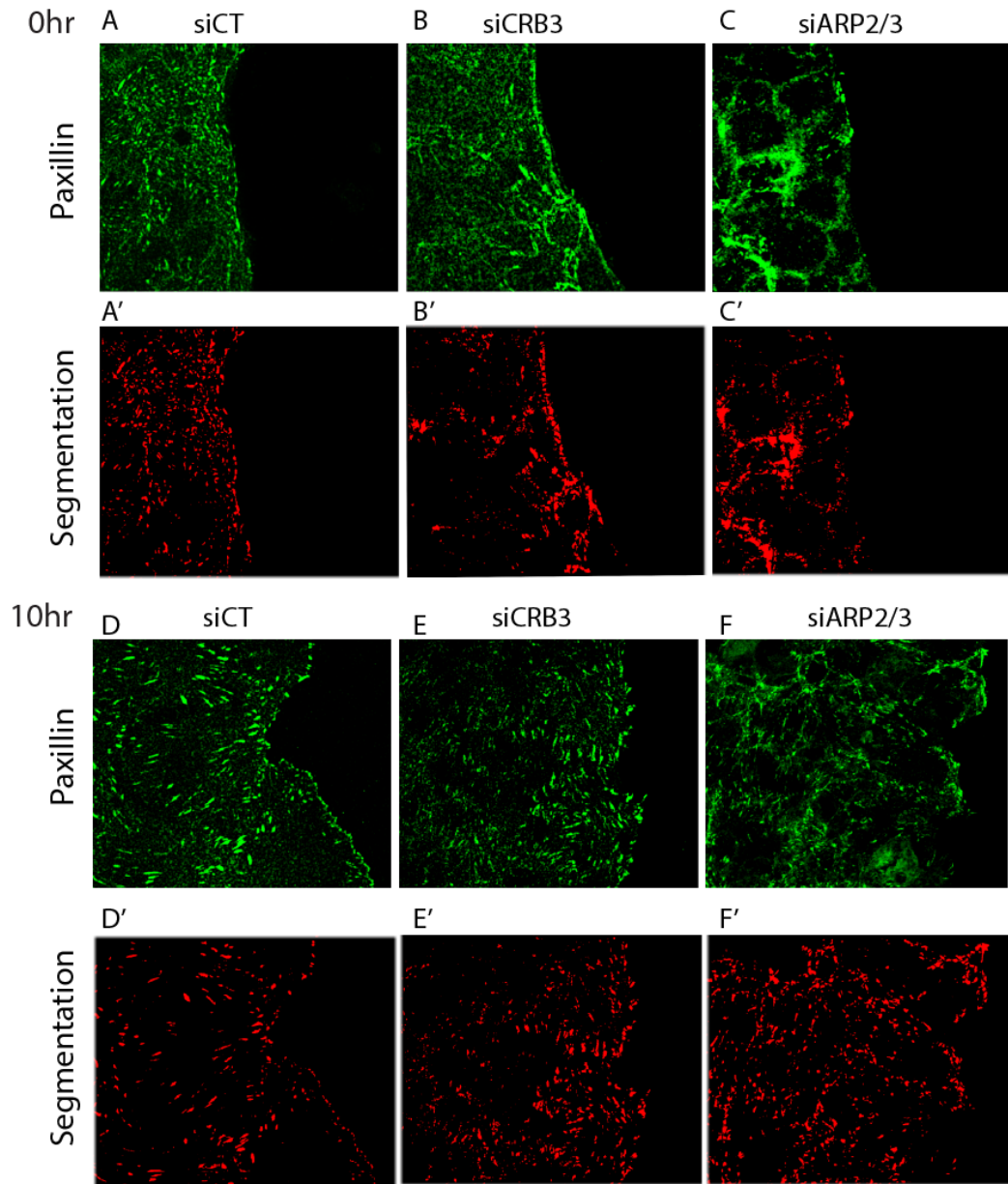


Figure S4



G Size based repartition Focal contacts

